The Role of Energy Scales for the Structure of Ionic Liquids at Electrified Interfaces - A Theory-Based Approach

Max Schammer,[1,2] Arnulf Latz,[1,2,3,*] and Birger Horstmann[1,2,3,†]

[1]*German Aerospace Center, Pfaffenwaldring 38-40, 70569 Stuttgart, Germany*
[2]*Helmholtz Institute Ulm, Helmholtzstraße 11, 89081 Ulm, Germany*
[3]*Universität Ulm, Albert-Einstein-Allee 47, 89081 Ulm, Germany*

Ionic liquids offer unique bulk and interfacial characteristics as battery electrolytes. Our continuum approach naturally describes the electrolyte on a macroscale. An integral formulation for the molecular repulsion, which can be quantitatively determined by both experimental and theoretical methods, models the electrolyte on the nanoscale. In this article, we perform a systematic series expansion of this integral formulation, derive a description of chemical potentials in terms of higher-order concentration gradients, and rationalize the appearance of fourth-order derivative-operators in modified Poisson equations, recently proposed in this context. In this way, we formulate a rigorous multi-scale methodology from atomistic quantum chemistry calculations to phenomenologic continuum models. We apply our generalized framework to ionic liquids near electrified interfaces and perform analytic asymptotic analysis. Three energy scales describing electrostatic forces between ions, molecular repulsion, and thermal motion determine the shape and width of the long-ranging charged double layer. We classify the charge screening mechanisms dependent on the system parameters dielectricity, ion size, interaction strength, and temperature. We find that the charge density of electrochemical double layers in ionic liquids either decays exponentially, for negligible molecular repulsion, or oscillates continuously. Charge ordering across several ion-diameters occurs if the repulsion between molecules is comparable with thermal energy and Coulomb interaction. Eventually, phase separation of the bulk electrolyte into ionic layers emerges once the molecular repulsion becomes dominant. Our framework predicts the exact phase boundaries between these three phases as function of temperature, dielectricity and ion-sizes.

I. INTRODUCTION

Strong electrostatic correlations in crowded environments play an important role in biology, chemistry and physics.[1–3] For example, in molecular biology, they account for DNA packing,[4] which is crucial for the compactification of genetic materials in viruses,[5] impact the cytoskeleton organization,[6] and influence transport in ion channels.[7] Furthermore, such correlations explain the thermodynamic stability of plasmas,[8,9] and charged colloidal suspensions.[10,11]

Surprisingly, the complexity of these phenomena can be understood to a large degree by models derived initially for electrolyte solutions.[12] Starting from the fundamental Debye-Hückel theory for dilute solutions,[13] increasingly accurate models for concentrated electrolytes were developed,[14] taking more complex Coulomb correlations into account.

As ionic liquids (ILs) consist only of positive and negative ions without neutral solvent, they constitute the extreme limit for the examination of electrostatic correlations in electrolytic solutions. Indeed, ILs possess characteristic properties in the bulk-regime,[15,16] but also near electrified interfaces.[17] This makes them highly attractive from both fundamental and applied perspectives.[18–24] The study of interfacial electrochemistry is of wide-ranging interest. For example, the behavior of ILs near electrified interfaces has paramount importance for their performance as battery electrolytes.[25,26]

Theoretical studies of ILs near electrified interfaces discuss the structure of charged electrochemical double layers

(EDL) on atomistic/molecular scales. These include classical density functional theory (cDFT) simulations, and molecular-dynamics (MD) simulations. cDFT gives detailed insights into the arrangement of molecules in the EDL.[27–29] MD resolves the molecular motion and can elucidate the EDL structure.[30–32]

However, cDFT/MD simulations are limited due to their computational costs. Simulations at length-scales above the nanometer scale are hardly accessible for the atomistic / molecular approach. Thus, continuum theories, and mean-field-theories (MFT) provide a complimentary methodology for the simulation of larger systems, where the microscopic details can be neglected, or are used as averaged parameters (*e.g.* constant dielectric parameters).

Usually, MFTs for electrolytes are based on lattice gas models of ions, first proposed by Bikermann.[33] Recently, these MFTs have attained great interest in the study for ILs. As proposed by Santangelo for aqueous systems,[34] the extension of MFTs by higher-order electrostatic correlations renders useful for the description of long-ranged structures emerging in electrolytes. Bazant, Storey and Kornyshev (BSK) applied this approach to ILs near electrified interfaces.[35] By using a phenomenological model, which is based on a generalized Ginzburg-Landau functional, BSK describe charge oscillations known as overscreening and charge saturation known as crowding. Yochelis et al. rationalized this approach, and extended it to bulk properties.[36–40] However, MFT models are usually restricted to equilibrium effects of binary ILs with structureless bulk, although rare MFT models, complemented by continuum methods[39,41] and extended to the ternary case[42] exist.

This highlights the advantage of continuum frameworks, which describe dynamical transport processes. In addition,

---

continuum models based on rigorous physical assumptions,[43] identify coupled phenomena arising from the interplay of mechanics, thermodynamics, and electromagnetic theory.[44] Furthermore, this approach allows to develop a unified, thermodynamically consistent framework, which provides the common theoretical basis for the description of different electrochemical systems.[45–49] Continuum models are not restricted to binary, or ternary systems, as they can be formulated for arbitrary many species, charged and uncharged. Thus, they apply to more realistic electrolytes.

Recently, we proposed such a novel continuum transport theory.[45] In this theory, we take account for steric effects via the mean-volume, which is due to finite molar volumes of the ion species. For this purpose, we impose a volume constraint on the electrolyte. This mechanism stabilizes the bulk structure against Coulomb collapse,[50] and leads to charge-saturation near electrified interfaces. Thus our theory resolves the deficiencies of the classical Poisson-Boltzmann (PB) theory, which predicts unrealistically high interface-concentrations.[14] Furthermore, the existence of finite molar volumes of the electrolyte species leads to a pressure dependence of the chemical potentials (in accordance with thermodynamic arguments).[51]

However, this bulk-framework cannot describe the emergence of long-range structures in ILs near electrified interfaces. Therefore, in a joint experimental / theoretical work, we extended our framework with non-local interactions, and validated it with results obtained from atomic-force-microscopy.[52] Thus, we extended the mean-volume-effect of the bulk theory with molecular volume exclusion due to hardcore repulsion. Our holistic framework allows to couple dynamic transport processes occurring in the bulk-electrolyte with interfacial electrochemical processes. Thus, we provide a continuum model which bridges the length-scales from nanometers, *e.g.*, EDL, to millimeters, *e.g.*, battery cells. Moreover, our framework allows to connect the continuum description with correlation functions generated by MD.

However, the dependence of EDL structures on molecular repulsion, molecular size, temperature, and dielectricity is still unknown. In this paper, we derive such an understanding with asymptotic analysis. To this aim, we present our thermodynamically consistent transport theory with an integral formulation of non-local interactions in section II A. These correlations represent atomistic volume exclusion and lead to modified constitutive equations (eqs. (2) to (5)). Moreover, the interactions impose contributions to the stress-tensor, and thus modify the mechanical coupling to the transport equations (eq. (6)). In section II B, we approximate the interaction functional with a gradient expansion, which facilitates the analytic asymptotic analysis of the EDL structure. In section II C, we apply our extended framework to study the EDL structure for neat ILs. When we non-dimensionalize our dynamical description in section II D, three competing energy scales describing electrostatic forces between ions, molecular repulsion, and thermal motion appear in the theory. Since our focus lies on the formation of equilibrium structures, we discuss the stationary state in section II E. In section II F, we discuss limiting cases of our stationary theory.

We perform numeric simulations and analytic asymptotic analysis to study the interplay and the effect of the competing energy scales on EDL structures. First, in section III, we discuss the EDL structure for the mean volume constraint. Second, in section IV, we incorporate molecular repulsion into our analysis and classify the EDL structure dependent on the relation between competing energy scales.

II. THEORY

A. Generalized Transport Theory

Recently, we have proposed a free energy functional $F^{\mathrm{b}} = \int \mathrm{d}V\, \rho \varphi_{\mathrm{H}}$ for the dynamical description of ionic liquids in the bulk-phase.[45] In this bulk-model, the Helmholtz free energy density $\varphi_{\mathrm{H}}(\Upsilon) = \varphi_{\mathrm{H}}(T, c_1, \ldots, c_{\mathrm{N}}, \boldsymbol{D}, \boldsymbol{\kappa})$ is a function of the variables temperature T, concentrations c_γ, dielectric displacement $\boldsymbol{D}$, and strain-rate tensor $\boldsymbol{\kappa}$. This variable-set Υ constitutes material-specific properties of multi-component, viscous and polarizable media in liquid state.

In contrast, models describing non-local interactions rely on functionals $F^{\mathrm{int}}[\Upsilon]$, such that the free energy takes the form

$$F[\Upsilon] = F^{\mathrm{int}}[\Upsilon] + F^{\mathrm{b}}(\Upsilon) = F^{\mathrm{int}}[\Upsilon] + \int \mathrm{d}V\, \rho \varphi_{\mathrm{H}}. \quad (1)$$

The following discussion relies on the derivation of our bulk transport theory, presented in Ref. 45. Here, we highlight all significant steps, and state the relevant, final results. In the SI (see section SI-1), we provide a more detailed discussion.

The extension of the free energy according to eq. (1) leads to modified constitutive equations for entropy density s, electric field strength $\mathcal{E}$, magnetic field $\mathcal{H}$, and chemical potentials μ_γ, via functional-derivatives (see section SI-1 A),

$$\rho s = -\rho \frac{\partial \varphi_{\mathrm{H}}}{\partial T} - \frac{\delta F^{\mathrm{int}}}{\delta T}, \quad (2)$$

$$\mathcal{E} = \rho \frac{\partial \varphi_{\mathrm{H}}}{\partial \boldsymbol{D}} + \frac{\delta F^{\mathrm{int}}}{\delta \boldsymbol{D}}, \quad (3)$$

$$\mathcal{H} = \rho \frac{\partial \varphi_{\mathrm{H}}}{\partial \boldsymbol{B}} + \frac{\delta F^{\mathrm{int}}}{\delta \boldsymbol{B}}, \quad (4)$$

$$\mu_\alpha = \frac{\partial (\rho \varphi_{\mathrm{H}})}{\partial c_\alpha} + \frac{\delta F^{\mathrm{int}}}{\delta c_\alpha}. \quad (5)$$

Equations (2) to (5) are supplemented by $\partial \varphi_{\mathrm{H}}/\partial \boldsymbol{\kappa} = \delta F^{\mathrm{int}}/\delta \boldsymbol{\kappa} = 0$, and by the constitutive equation for the stress tensor,

$$\boldsymbol{\sigma} = \boldsymbol{\tau} - \left(\sum_{\alpha=1}^{\mathrm{N}} c_\alpha \left[\frac{\partial (\rho \varphi_{\mathrm{H}})}{\partial c_\alpha} + \frac{\delta F^{\mathrm{int}}}{\delta c_\alpha} \right] - \rho \varphi_{\mathrm{H}} + \mathcal{E} \boldsymbol{D} + \mathcal{H} \boldsymbol{B} \right) \mathbf{Id}$$
$$+ \mathcal{E} \otimes \boldsymbol{D} + \mathcal{H} \otimes \boldsymbol{B}. \quad (6)$$

Here $\boldsymbol{\tau}(\boldsymbol{\kappa}) = \lambda \nabla \cdot \mathbf{v} \cdot \mathbf{Id} + 2\eta \cdot \boldsymbol{\kappa}_{\mathrm{tf}}$ describes the viscosity tensor, where $\boldsymbol{\kappa} = \mathrm{grad}\, \mathbf{v} + (\mathrm{grad}\, \mathbf{v})^{\mathrm{T}} = \nabla \mathbf{v} \cdot \mathbf{Id}/3 + \boldsymbol{\kappa}_{\mathrm{tf}}$ is the strain-rate tensor and $\mathbf{v}$ is the center-of-mass convection velocity.[45]

For the remaining part of this work, we neglect thermal driving forces by setting the temperature to constant values,

and assume the electrostatic limit $\boldsymbol{B} = 0$ and $\mathcal{H} = 0$. This determines the electric field $\boldsymbol{E} = \boldsymbol{\mathcal{E}}$ by the electrostatic potential, $\boldsymbol{E} = -\nabla\Phi$.

We evaluate our framework for the bulk-energy of a linear dielectric medium discussed in Ref. 45.

$$\rho\varphi_{\mathrm{H}} = \frac{\boldsymbol{ED}}{2} + \frac{\mathcal{K}}{2}\left(1 - \sum_{\alpha=1}^{N} \nu_\alpha^0 c_\alpha\right)^2 + RT \sum_{\alpha=1}^{N} c_\alpha \ln(c_\alpha \nu_\alpha), \quad (7)$$

where the electric field is $\boldsymbol{E} = \boldsymbol{D}/\varepsilon_0\varepsilon_{\mathrm{R}}$. The second term comprises volumetric energy contributions. We express this term by expansion around a stable reference configuration parameterized by ν_α^0 and $\mathcal{K}$ constitutes a Lagrange multiplier. To take account for asymmetric volumes of the ions, we express the entropy of mixture using volume fractions $c_\alpha \nu_\alpha$, instead of mole fractions c_α/c.[39] This "Flory-Huggins"-approach is based on a modified statistics,[53] which favours equal volumes for each species instead of equal number of molecules, and accounts for the averaged impact of strong short range repulsions on particle distributions. Within the framework Ref. 45 this change is captured by the bulk activity coefficients f_α given by the partial molar volumes $f_\alpha = \nu_\alpha$.

In Ref. 45 we show that the chemical potentials

$$\mu_\alpha = RT\left(1 + \ln c_\alpha \nu_\alpha\right) + \frac{\delta F^{\mathrm{int}}}{\delta c_\alpha} - \mathcal{K}\nu_\alpha^0\left(1 - \sum_{\beta=1}^{N} c_\beta \nu_\beta^0\right), \quad (8)$$

depend on elastic properties through the last term. As discussed in our previous work[45] and in Ref. 54 for hardly compressible electrolytes, this elastic energy represents a linear pressure contribution and the Lagrange multiplier $\mathcal{K}$ is found to be the Bulk modulus. In this work, we assume the incompressible limit $\mathcal{K}\to\infty$. This implies that the thermodynamic partial molar volumes ν_α become pressure independent and approach the partial molar volumes in the reference state,

$$\lim_{\mathcal{K}\to\infty} \nu_\alpha = \nu_\alpha^0. \quad (9)$$

We take account for local conservation of volume via the Euler equation for the volume,

$$\sum_{\alpha=1}^{N} c_\alpha \nu_\alpha = 1. \quad (10)$$

The elastic term in the chemical potentials (see eq. (8)) is constrained by the assumption of mechanical equilibrium $\mathrm{div}\,\boldsymbol{\sigma} = 0$. Then, eq. (6) implies $\mathcal{K}\sum_{\beta=1}^{N} \nu_\beta \cdot \nabla c_\beta = -\varrho\nabla\Phi - RT \cdot \nabla c - \nabla \sum_{\beta=1}^{N} c_\beta \cdot \delta F^{\mathrm{int}}/\delta c_\beta$ and the electrochemical forces $\nabla\mu_\alpha^{\mathrm{el}} = \nabla\mu_\alpha + Fz_\alpha\nabla\Phi$ become

$$\nabla\mu_\alpha^{\mathrm{el}} = \nu_\alpha \cdot \nabla\boldsymbol{\tau} + \sum_{\beta=1}^{N}\left(\delta_\alpha^\beta - \nu_\alpha c_\beta\right) \cdot \nabla\left(Fz_\beta\Phi + \frac{\delta F^{\mathrm{int}}}{\delta c_\beta}\right) +$$
$$+ RT\left(\nabla\ln\left[c_\alpha\nu_\alpha\right] - \nu_\alpha\nabla c\right), \quad (11)$$

where $\nabla\boldsymbol{\tau} = (\lambda + \eta/3)\nabla(\nabla\mathbf{v}) + \eta \cdot \nabla^2\mathbf{v}$.

Thus, in this limit, we obtain inter-species couplings, in agreement with the Gibbs-Duhem relation,

$$\sum_{\alpha=1}^{N} c_\alpha \cdot \nabla\mu_\alpha^{\mathrm{el}} = \nabla\boldsymbol{\tau}. \quad (12)$$

B. Gradient Expansion of Molecular Interactions

Recently,[52] we proposed a model for hardcore-interactions based on a convolution-functional for the interaction free energy,

$$F^{\mathrm{int}} = \frac{1}{2}\sum_{\alpha,\beta}^{N} \iint \mathrm{d}x^3\mathrm{d}y^3\, \mathcal{F}_{\alpha\beta}(|\mathbf{x} - \mathbf{y}|)c_\alpha(\mathbf{x})c_\beta(\mathbf{y}), \quad (13)$$

leading to transport contributions in the form (see section SI-1 C)

$$\frac{\delta F^{\mathrm{int}}}{\delta c_\alpha}(\mathbf{x}) = \sum_{\beta}^{N} \int \mathrm{d}y^3\, \mathcal{F}_{\alpha\beta}(|\mathbf{x} - \mathbf{y}|)c_\beta(\mathbf{y}). \quad (14)$$

The symmetric potentials $\mathcal{F}_{\alpha\beta}$ determine the correlation length ℓ_{int}, and the magnitude of the interaction. The number of additional parameters describing this interaction depends upon the model for $\mathcal{F}_{\alpha\beta}$. In a previous publication, for example, we used a Lennard-Jones-type force-field for $\mathcal{F}_{\alpha\beta}$.[52] Such potentials are often used in the literature.[55–59] Furthermore, since

$$\frac{\delta^2 F^{\mathrm{int}}}{\delta c_\gamma(\mathbf{z})\delta c_\alpha(\mathbf{x})} = \mathcal{F}_{\alpha\gamma}(|\mathbf{x} - \mathbf{z}|), \quad (15)$$

the potentials $\mathcal{F}_{\alpha\gamma}$ determine the direct pair correlation functions used in liquid state theory.[50]

Experimental results suggest that such interactions typically decay after some ionic diameters.[52] Thus, we focus on potentials $\mathcal{F}_{\alpha\beta}$ ranging over the size of one molecule. Their extend ℓ_{int} is large compared to the exponential decay of the electric field, i.e., the Debye-length,[60,61] yet small compared to the battery cell.

In the SI (see section SI-1 B), we show that such convolution functionals F^{int} can be approximated in power-series of concentration gradients, when $\mathcal{F}_{\alpha\beta}$ is short-ranged,

$$F^{\mathrm{int}}[c_\gamma] = \frac{1}{2}\sum_{\alpha,\beta}^{N}\sum_{n=0}^{\infty} \Gamma_{\alpha\beta}^{2n} \int \mathrm{d}^3y\, c_\alpha(y) \cdot \nabla^{2n}c_\beta(y), \quad (16)$$

where

$$\Gamma_{\alpha\beta}^n(\mathcal{F}_{\alpha\beta}) = \frac{1}{n!} \cdot \int \mathrm{d}^3x\, \mathcal{F}_{\alpha\beta}(|x|) \cdot x^n. \quad (17)$$

Here, $\Gamma_{\alpha\beta}^n$ are symmetric perturbation coefficients of dimension $[\Gamma_{\alpha\beta}^{2n}] = \mathrm{J\,m}^{3+2n}\mathrm{mol}^{-2}$. With this Ansatz, the complete free energy functional for IL electrolytes becomes

$$F = \int \mathrm{d}V \left[\frac{\boldsymbol{ED}}{2} + RT \sum_{\alpha=1}^{N} c_\alpha \ln(c_\alpha \nu_\alpha) + \frac{\mathcal{K}}{2}\left(1 - \sum_{\alpha=1}^{N} c_\alpha \nu_\alpha\right)^2 \right.$$
$$\left. + \frac{1}{2}\sum_{\alpha,\beta}^{N}\sum_{n=0}^{\infty} \Gamma_{\alpha\beta}^{2n}c_\alpha \cdot \nabla^{2n}c_\beta \right]. \quad (18)$$

The functional derivative in eq. (5) determines the excess chemical potentials due to the interaction (see section SI-1 C),

$$\frac{\delta F^{int}}{\delta c_\alpha(z)} = \sum_{\beta=1}^{N}\sum_{n=0}^{\infty} \Gamma_{\alpha\beta}^{2n} \cdot \nabla^{2n}c_\beta(z). \quad (19)$$

The corresponding electrochemical potentials for ionic liquid electrolytes are

$$\nabla\mu_\gamma^{\text{el}} = \left(Fz_\gamma - \nu_\gamma\varrho\right)\nabla\Phi + RT\cdot(\nabla c_\gamma)/c_\gamma - RT\nu_\gamma\nabla c$$

$$+ \sum_{n=0}^{\infty}\sum_{\alpha,\beta}^{N}\left(\delta_\alpha^\gamma - \nu_\gamma c_\alpha\right)\Gamma_{\alpha\beta}^{2n}\cdot\nabla^{2n+1}c_\beta. \quad (20)$$

We specify our electrolyte model and assume a one-dimensional Gaussian interaction potential for symmetric ions,

$$\mathcal{F}_{\alpha\beta} = \left(2\sqrt{2\pi}\right)^3\cdot\mathcal{V}^0\cdot(N_A)^2\cdot\exp\left[-2\left(\frac{x\pi}{a}\right)^2\right]. \quad (21)$$

Here, $\mathcal{V}^0$ denotes the characteristic interaction energy, and a is the extension of ion-pairs. This material parameter determines the correlation length $\ell_{\text{int}} = a/\pi\sqrt{2}$ of the interaction. We assume that a emerges naturally from the common molar volume $\nu = \nu_+ + \nu_-$ via $\nu = N_A a^3$, which is justified below (see section IV A 2 and eq. (63)). Thus, only $\mathcal{V}^0$ is introduced as a novel independent material parameter. In contrast, potentials of Lennard Jones type need at least one more parameter for the well-depth. In the case of a binary system, the lowest order expansion coefficients (see eq. (17)) of the inter-species correlations for the Gaussian model in eq. (21) are (see section SI-3 D 1)

$$\Gamma_{12}^0 = \mathcal{V}^0 N_A\nu = \mathcal{V}^0\left(N_A\right)^2 a^3, \quad (22)$$

$$\Gamma_{12}^2 = \frac{\ell_{\text{int}}^2}{2}\cdot\Gamma_{12}^0 = \frac{a^2}{4\pi^2}\cdot\Gamma_{12}^0. \quad (23)$$

C. Binary IL

In this section, we apply our formalism to binary ILs at electrified interfaces. Thus, we use the extended electrochemical forces eq. (20) in our multicomponent framework derived in Ref. 45.

As discussed in section II A, binary electrolytes are described with the variables electric potential Φ, charge density ϱ, and center-of-mass convection velocity $\mathbf{v}$. Furthermore, the electric conductivity κ is the only independent transport parameter in this case.[45] The dynamical transport equations are

$$\partial_t\varrho = -\nabla\left(\varrho\mathbf{v}\right) - \nabla\mathcal{J}, \quad (24)$$

$$\varrho = -\varepsilon_0\nabla\varepsilon_R\nabla\Phi, \quad (25)$$

$$\nabla\mathbf{v} = (M_+\nu_- - M_-\nu_+)/Fz_+M_{\text{IL}}\cdot\nabla\mathcal{J}. \quad (26)$$

Here, $M_\pm$ are the molar masses of the ionic species which sum to M_{IL}, and $\mathcal{J}$ is the electric current relative to the center-of-mass motion, $\mathcal{J} = \kappa(M_+\cdot\nabla\mu_-^{\text{el}} - M_-\nabla\mu_+^{\text{el}})/M_{\text{IL}}Fz_+$.

Solutions to eqs. (24) to (26) determine the ionic concentrations via $\varrho = Fz_+(c_+ - c_-)$ (charge-conservation), and via the Euler equation for the volume eq. (10).

We restrict our set-up to one spatial dimension, and assume that the inert electrified interface is located at $x = 0$. The electroneutral boundary condition $\varrho(x\to\infty) = 0$ implies that the bulk concentration $c^{\text{b}} = c_\pm(x\to\infty)$ is completely determined
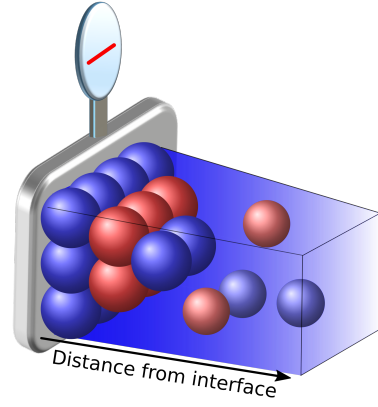

FIG. 1. Scheme of the as-modelled set-up. The binary IL-electrolyte PYR[1,4]TFSI is subject to the negatively charged interface at the left, which causes the formation of an electrochemical double layer (EDL). Charge-ordering diminishes with increasing distance from the interface (towards the right side), and the electrolyte is electroneutral in the bulk.

by the total partial molar volume $\nu = \nu_+ + \nu_-$ via $c^{\text{b}}\cdot\nu = 1$. Since binary ILs are electrically neutral, $z_+ = -z_+$, and we choose $z_+ > 0$.

We neglect viscous forces in our discussion of the EDL ($\nabla\tau = 0$). Therefore, the Gibbs-Duhem relation (see eq. (12)) becomes $c_+\nabla\mu_+^{\text{el}} + c_-\nabla\mu_-^{\text{el}} = 0$, and the expression for the electric flux simplifies to $\mathcal{J} = -\kappa\nu\rho/Fz_+M_{\text{IL}}\cdot\nabla\mu_{\text{IL}}$, where we use the chemical potential of the anion-species to determine the IL-electrolyte ($\nabla\mu_{\text{IL}} = \nabla\mu_-^{\text{el}}$),

$$\nabla\mu_{\text{IL}} = \nabla\left(Fz_+\Phi - \gamma_+\frac{\delta F^{\text{int}}}{\delta c_-} + \gamma_-\frac{\delta F^{\text{int}}}{\delta c_+} - RT\gamma_+\ln\left[c_-/c^{\text{b}}\right]\right.$$

$$\left. + RT\gamma_-\ln\left[c_+/c^{\text{b}}\right]\right). \quad (27)$$

Here, we introduced the relative magnitude of the molar volumes $\gamma_\pm = \nu_\pm/\nu$. Thus, the forces given by eq. (27) depend upon the model for F^{int}. Furthermore, using the Gauss-model (see eq. (21)), we can either close the forces via the "complete" integral equation (eq. (14)), or using the gradient expansion (eq. (19)).

We want to apply the half-cell potential $\Delta\phi$. Since the electric potential Φ is continuous across the electrode-electrolyte interface, $\Phi(0)$ in the electrolyte is subject to the boundary condition

$$\Phi(0) - \Phi(x\to\infty) = \Delta\phi. \quad (28)$$

Without loss of generality, we set the electrolyte potential in the bulk to zero, $\lim_{x\to\infty}\Phi = 0$. Hence, $\Delta\phi = \Phi(0)$ is the potential applied to the electrode.

We perform one-dimensional numeric simulations of this system of equations eqs. (24) and (25) in the completely dissociated state, subject to an inert electrified interface (for more details, see section SI-4 A). This electrolyte is part of the IL-family comprised of TFSI anions and PYR cations. Due to their excellent electrochemical properties, these ILs are widely studied and used for applications in lithium-ion

batteries.[62] We state the electrolyte parameters in the SI (see section SI-4 B).

D. Energy Scales and Dimensions

We introduce dimensionless variables for electric potential, $\tilde{\Phi} = \Phi \cdot Fz_+/RT$, and charge density, $\tilde{\varrho} = \varrho\nu\tilde{c}^b/Fz_+$, where $\tilde{c}^b = (\gamma_+)^2 + (\gamma_-)^2$ is the dimensionless electroneutral bulk state, corresponding to $c^b = 1/\nu$. In accordance with these definitions, we introduce $\tilde{c}_\alpha = c_\alpha\nu\tilde{c}^b$ such that $\tilde{\varrho} = \tilde{c}_+ - \tilde{c}_-$. Hence, the Euler equation for the volume becomes $\tilde{c}^b = \gamma_+\tilde{c}_+ + \gamma_-\tilde{c}_-$. Via this gauge, the saturation threshold, corresponding to maximal ion-concentration, is completely determined by the relative volume-size alone, $\tilde{c}^{sat} = \tilde{c}^b/\gamma_{\alpha^\star}$, where $\alpha^\star$ denotes the saturation species. Furthermore, we use system parameters to define the time-scale $\varepsilon_0\varepsilon_R/\kappa$, and introduce a dimensionless time-derivative $\partial_{\tilde{t}} = \varepsilon_0\varepsilon_R/\kappa \cdot \partial_t$. The center-of-mass convection velocity in it's non-dimensionalized form reads $\tilde{\mathbf{v}} = \varepsilon_0\varepsilon_R/L_D\kappa\chi \cdot \mathbf{v}$. Here, $\chi = (M_+\gamma_- - M_-\gamma_+)/M_{IL}\tilde{c}^b$ measures the "asymmetry" of the ion-species. In the SI (see section SI-2), we motivate our choice of non-dimensionalized quantities.

The Poisson equation suggests defining the generalized Debye-length

$$L_D = \sqrt{\frac{k_B T \varepsilon_0\varepsilon_R a^3 \tilde{c}^b}{(ez_+)^2}}. \tag{29}$$

Here, we used $F = eN_A$ for the Faraday constant, where e is the elementary charge, and N_A is Avogadro's constant, and the model $\nu = N_A a^3$ for the partial molar volumes introduced above. This Debye-length differs from the canonical definition by the asymmetry-factors $\gamma_\pm$.[63] However, it reproduces the textbook definition for symmetric ions ($\gamma_\pm = 0.5$). L_D becomes minimal for $\gamma_\pm = 0.5$ because the mixing entropy of a binary electrolyte is extremal for equal ion-size. Thus, asymmetry increases the Debye-screening length.

With this length scale, we non-dimensionalize our grid, *viz.* $\tilde{x} = x/L_D$ and $\tilde{\nabla} = L_D \cdot \nabla$, and obtain the dimensionless Poisson-equation,

$$\tilde{\varrho} = -\tilde{\nabla}^2 \tilde{\Phi}. \tag{30}$$

This yields non-dimensionalized electrostatic fields $\tilde{\mathbf{D}} = a\tilde{c}^b\mathbf{D}/L_D ez_+$ and $\tilde{\mathbf{E}} = L_D ez_+\mathbf{E}/k_B T$, such that $\tilde{\varrho} = \tilde{\nabla}\tilde{\mathbf{D}}$, $\tilde{\mathbf{E}} = -\tilde{\nabla}\tilde{\Phi}$, and $\tilde{\mathbf{D}} = \tilde{\mathbf{E}}$.

Our theory also contains a generalized Bjerrum-length L_B, which measures the distance at which the electrostatic energy and the thermal energy become comparable,

$$L_B = \frac{(ez_+)^2}{k_B T \varepsilon_0\varepsilon_R \tilde{c}^b} = \frac{a^3}{L_D^2}. \tag{31}$$

Next, we non-dimensionalize the transport equations for the binary, symmetric IL (see eqs. (24) and (26)). The corresponding non-dimensional current flux takes the form $\tilde{\mathcal{J}} = -(1 + \chi\tilde{\varrho})\tilde{\nabla}\tilde{\mu}_{IL}$, where the non-dimensionalized chemical forces $\tilde{\nabla}\tilde{\mu}_{IL} = 1/RTL_D \cdot \nabla\mu_{IL}$ are subject to the two descriptions eqs. (14) and (19), see also eq. (27). Thus, we find

$\partial_{\tilde{t}}\tilde{\varrho} = \tilde{\nabla}[(1 + \chi\tilde{\varrho})\tilde{\nabla}\tilde{\mu}_{IL}] - \chi\tilde{\nabla}(\tilde{\varrho}\tilde{\mathbf{v}})$ and $\tilde{\nabla}\tilde{\mathbf{v}} = -\tilde{\nabla}[(1 + \chi\tilde{\varrho})\tilde{\nabla}\tilde{\mu}_{IL}]$. However, since we neglect convective effects in our EDL discussion, the complete set of equations consists of the Poisson equation and one transport equation for the charges. In non-dimensionalized form, the transport equation in the integral description follows by substituting eq. (14) into eq. (27)

$$\partial_{\tilde{t}}\tilde{\varrho} = \tilde{\nabla}\Bigg[(1 + \chi\tilde{\varrho}) \cdot \tilde{\nabla}\bigg(\tilde{\Phi} - \gamma_+ \ln\big[\tilde{c}_-/\tilde{c}^b\big] + \gamma_- \ln\big[\tilde{c}_+/\tilde{c}^b\big] - \\ - \int d\tilde{x}^3 \tilde{\mathcal{F}}_{\alpha\beta}(|\tilde{\mathbf{x}} - \tilde{\mathbf{y}}|)\tilde{\varrho}(\tilde{\mathbf{y}})\bigg)\Bigg], \tag{32}$$

where we introduced two energy scales for thermal energy E_{th} and electrostatic energy E_{el},

$$E_{th} = k_B T \cdot \frac{\tilde{c}^b}{2\gamma_+\gamma_-}, \tag{33}$$

$$E_{el} = \frac{(ez_+)^2}{4\pi\varepsilon_0\varepsilon_R} \cdot \frac{1}{4\gamma_+\gamma_-} \cdot \frac{1}{a}. \tag{34}$$

In the case of symmetric ions $\gamma_\pm = 0.5$, these energy scales take the textbook form for thermal energy and Coulomb energy of charges at distance a. Apparently, both energy scales are coupled by the generalized Debye-length L_D,

$$\frac{E_{th}}{E_{el}} = 8\pi\left(\frac{L_D}{a}\right)^2. \tag{35}$$

In eq. (32), we used these two energy-scales to non-dimensionalize the interaction potential,

$$\tilde{\mathcal{F}} = \sqrt{\frac{E_{th}}{8\pi E_{el}}}\frac{\mathcal{F}/(N_A)^2}{8\pi E_{el}} = \frac{\mathcal{V}^0}{E_{el}}\sqrt{\frac{E_{th}}{E_{el}}}\exp\left(-2\left[\frac{x\pi}{a}\right]^2\right). \tag{36}$$

The integral form eq. (32) for the transport equation allows to relate our continuum framework to MD-simulations as discussed in section V A.

The energy scales E_{th} and E_{el} non-dimensionalize the perturbation-modes (see eq. (17)),

$$\tilde{\Gamma}_{+-}^{2n} = \frac{\Gamma_{+-}^{2n}}{E_{th}a^3(L_D)^{2n}(N_A)^2}. \tag{37}$$

However, since we restrict the gradient-expansion of the interaction to the trivial and first non-trivial modes ($\tilde{\Gamma}_{+-}^0 = \mathcal{V}^0/E_{th}$ and $\tilde{\Gamma}_{+-}^2 = 2/\pi \cdot \mathcal{V}^0/E_{th} \cdot E_{el}/E_{th}$), we obtain for the non-dimensionalized transport equation in the gradient description

$$\partial_{\tilde{t}}\tilde{\varrho} = \tilde{\nabla}\Bigg[(1 + \chi\tilde{\varrho}) \cdot \tilde{\nabla}\bigg(\tilde{\Phi} - \gamma_+ \ln\big[\tilde{c}_-/\tilde{c}^b\big] + \gamma_- \ln\big[\tilde{c}_+/\tilde{c}^b\big] - \\ - \frac{\mathcal{V}^0}{E_{th}}\left(1 + \frac{2}{\pi}\frac{E_{el}}{E_{th}} \cdot \tilde{\nabla}^2\right)\tilde{\varrho}\bigg)\Bigg]. \tag{38}$$

E. Stationary State

Since our focus lies on the formation of equilibrium structures, we discuss the system of equations in the stationary

limit. This allows to integrate the differential equations using electroneutral boundary conditions, which results in a simplified description susceptible to analytic techniques.

Stationarity ($\partial_t \varrho = 0$) implies that all fluxes are constant. Here, we have no flux conditions $\tilde{\mathcal{J}} = \tilde{\mathbf{v}} = 0$, which implies that both species are in equilibrium, $\nabla \mu_+^{el} = \nabla \mu_-^{el}$, *i.e.*,

$$\tilde{\nabla} \tilde{\mu}_{IL} = 0. \tag{39}$$

Thus, the stationary state for the binary electrolyte is described by the Poisson equation and eq. (39). Here, we evaluate the equilibrium condition using the gradient description (eq. (27)) in the non-dimensionalized form (see eqs. (37) and (38)), and integrate the result using electroneutral boundary conditions in the bulk,

$$0 = \tilde{\Phi} - \frac{\mathcal{V}^0}{E_{th}} \left(1 + \frac{2}{\pi} \frac{E_{el}}{E_{th}} \tilde{\nabla}^2 \right) \tilde{\varrho} - \left(\gamma_+ \ln \left[\frac{\tilde{c}_-}{\tilde{c}^b} \right] - \gamma_- \ln \left[\frac{\tilde{c}_+}{\tilde{c}^b} \right] \right). \tag{40}$$

Apparently, in contrast to the dynamical case where electrolyte momentum is important, the molar masses appearing as parameters in the fluxes $\mathbf{v}$ and $\mathcal{J}$ become irrelevant in the stationary limit. Instead, the relative magnitude of the molar volumes $\gamma_\pm$ enters the system of equations. This highlights the principal role of molar volumes as parameters in the stationary state and is a consequence of the Euler equation for the volume, eq. (10).

For completeness, we state the integral transport equation 32 in the stationary limit (see section SI-3 A)

$$0 = \tilde{\Phi} - \int d\tilde{y} \tilde{\mathcal{F}}_{+-} (\tilde{x}, \tilde{y}) \, \tilde{\varrho}(\tilde{y}) - \left(\gamma_+ \ln \left[\frac{\tilde{c}_-}{\tilde{c}^b} \right] - \gamma_- \ln \left[\frac{\tilde{c}_+}{\tilde{c}^b} \right] \right). \tag{41}$$

F. Small and Large Potentials

Equation (30) and eq. (40) (or eq. (41)) constitute the complete set of equations, necessary to describe a binary IL-electrolyte in stationary state. In section III A and section IV C, we solve these equations using numeric methods. Our goal is to supplement these numerical methods by an analytic examination of the gradient description. However, the analytic solution of the gradient description is hindered by the higher order gradients appearing in eq. (40) and by the different prefactors of the logarithmic terms (in general, $\gamma_+ \neq \gamma_-$). Therefore, we distinguish different limiting cases in our analysis in sections III B and IV A. In the SI, we describe the special case of symmetric ion-species (see sections SI-3 B and SI-3 C 3).

In section III B we motivate that the limiting case of small charge-densities, $\tilde{\varrho} \ll 1$, renders useful. In this case, we can expand the logarithmic term in eq. (40) and eq. (41) around the electroneutral state,

$$\gamma_+ \ln \left(\tilde{c}_- / \tilde{c}^b \right) - \gamma_- \ln \left(\tilde{c}_+ / \tilde{c}^b \right) \approx -\tilde{\varrho}, \tag{42}$$

such that eqs. (30) and (40) become

$$\tilde{\varrho} = -\tilde{\nabla}^2 \tilde{\Phi}, \tag{43}$$

$$0 = \tilde{\Phi} + \hat{\varepsilon}_R \tilde{\varrho}, \tag{44}$$

where $\hat{\varepsilon}_R$ is defined as dielectric operator

$$\hat{\varepsilon}_R = 1 - \sum_{n=0}^{1} \tilde{\Gamma}_{+-}^{2n} \cdot \tilde{\nabla}^{2n} = 1 - \frac{\mathcal{V}^0}{E_{th}} - \frac{2}{\pi} \cdot \frac{\mathcal{V}^0}{E_{th}} \cdot \frac{E_{el}}{E_{th}} \cdot \tilde{\nabla}^2. \tag{45}$$

In the absence of molecular repulsion, $\mathcal{V}^0 = 0$, the dielectric operator reduces to the canonical, scalar-valued dielectric parameter $\hat{\varepsilon}_R \to 1$.

Furthermore, quantities similar to $\hat{\varepsilon}_R$ also arise in the liquid state theory of classical statistical mechanics. This expansion corresponds to a small wave vector expansion of the dielectric function expressed as correlation function of the molecular dipole densities (see, e.g., Ref. 50).

In the following sections, we show that the gradient expansion, eqs. (43) and (44), allows significant insights into the competing effects of the interactions $\mathcal{V}^0$, E_{el}, E_{th}, and predicts the EDL structure as function of the parameters temperature, dielectricity, ion-size, and interaction strength.

III. MEAN STERIC EFFECT: CHARGE SATURATION

In this section, we neglect non-local interactions, $\mathcal{V}^0 = 0$, and discuss the EDL structure of the electrolyte due to bulk effects alone based on F^b (see eq. (1)). In this way, we reveal the competition between Coulombic ordering and entropic disordering, i.e., diffusion.

To this aim, we consider the system of equations constituted by the Poisson eq. (30) and eq. (40) subject to $\mathcal{V}^0 = 0$,

$$0 = \tilde{\Phi} - \gamma_+ \ln \left(\tilde{c}_- / \tilde{c}^b \right) + \gamma_- \ln \left(\tilde{c}_+ / \tilde{c}^b \right). \tag{46}$$

First, in section III A, we solve this system of equations numericaly. We supplement this investigation by an analytic analysis, and focus on the two limiting regimes of large and small electric potentials; in section III B 1 we discuss the case $\tilde{\Phi} \ll 1$, and in section III B 2 we discuss the case $\tilde{\Phi} \gg 1$. For the special case of symmetric ion-species ($\gamma_\pm = 0.5$), we derive an analytic solution for the electric field $\tilde{E}(\tilde{\Phi})$, and for the charge density $\tilde{\varrho}(\tilde{\Phi})$ as functions of the electrolyte electric potential in the SI (see section SI-3 C 3).

A. Simulations

Figure 2 shows numeric results for the system of eqs. (30) and (46). Figure 2a and fig. 2b illustrate screening profiles of the electric potential, the charge density, and the ion concentrations for varying electrode potentials $\Delta\phi$.

Apparently, the application of a negative electrode potential ($\Delta\phi < 0$) polarizes the electrolyte. The electric potential (see fig. 2a) is continuous across the interface and decays smoothly towards the electroneutral bulk region. The inset of fig. 2a shows that, for low electrode potentials, the charge density decays exponentially. A similar behavior can be observed in fig. 2b for the concentrations. The concentration of positive counter-ions increases towards the interface, whereas negative like-ions get depleted. Apparently, the electrolyte screens the
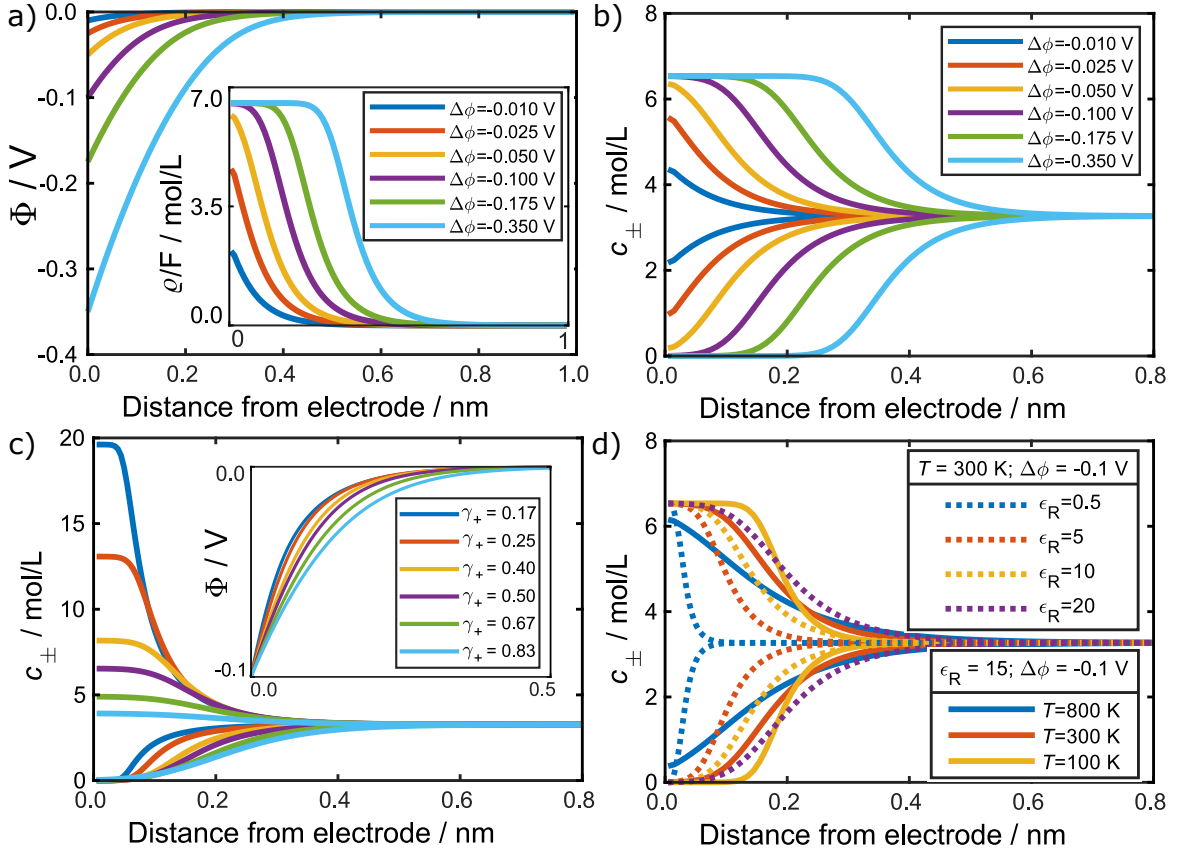
FIG. 2. Simulation results of the EDL structure perpendicular to the electrode-electrolyte interface for a binary IL (see eqs. (30) and (46)). If not mentioned otherwise, $T = 300$ K, $\varepsilon_R = 15$, and $\Delta\phi = -0.1$ V. a) Profiles of electric potential and charge density (inset) for different electrode potentials $\Delta\phi$. b) Concentration profiles of the anions and cations for different electrode potentials $\Delta\phi$. c) Concentration profiles for different volume ratios γ_+. The inset shows the corresponding electric potential. d) Concentration profiles for varying dielectric constants (dashed lines) and temperatures (solid lines).

electrode potential by accumulation of counter-ions. However, above $\Delta\phi \approx -0.05$ V, the counter-ion concentration saturates near the interface. A further increase of $\Delta\phi$ broadens the EDL.

This behavior can be explained by the mean volume effect. The application of a negative potential $\Delta\phi$ implies that positive ions accumulate near the interface, and negative ions deplete. However, the Euler equation for the volume, eq. (10), implies the saturation concentration $c_+^{\text{sat}} = 1/\nu_+$. Once the accumulated species reaches this saturation, the screening mechanism transitions from increasing the concentration at the interface to broadening the width of the EDL. The simulated EDL approaches a thickness of 0.6 nm at $\Delta\phi \approx -0.05$ V, which is significantly wider than predicted by the canonical Debye-Hückel-theory with the Debye length $L_D \approx 0.7$ Å (see eq. (29)). This phenomenon is typically denoted "crowding".[35]

Since the saturation concentration depends upon the molar volume, $c_\alpha^{\text{sat}} = 1/\nu_\alpha$, the partial molar volumes directly affect the screening behavior. Figure 2c shows numeric results for the ionic concentrations at different volume ratios $\gamma_\pm = \nu_\pm/\nu$ (ν is kept fixed). The EDL is thinner for smaller γ_+, as this allows for tighter packing of cations.

The effect of temperature T and dielectricity ε_R on the EDL structure is illustrated in fig. 2d. The screening is more effective for smaller values of ε_R and the EDL width increases with increasing magnitude of ε_R. This is in qualitative agreement with the screening behavior for dilute solutions as predicted by the Debye-Hückel theory. Likewise, the EDL becomes more diffuse with increasing temperature because of the disordering effect of thermal motion. The observed effects of T and ε_R highlight the competing interplay between the electrostatic effect of charge ordering and the disordering effect of entropy.

To summarize, the simulations show two distinct regimes of EDL structure. First, for large electrode potentials, $\Delta\tilde{\phi} \gg 1$, the charge is saturated near the interface. Second, near the electroneutral bulk region, where $\Delta\tilde{\phi} \ll 1$, the charge density decays exponentially. These two distinct EDL structures, charge saturation and exponential decrease, correspond to two disjoint electrolyte regimes, $|\tilde{\Phi}| \gg 1$ and $|\tilde{\Phi}| \ll 1$, respectively.
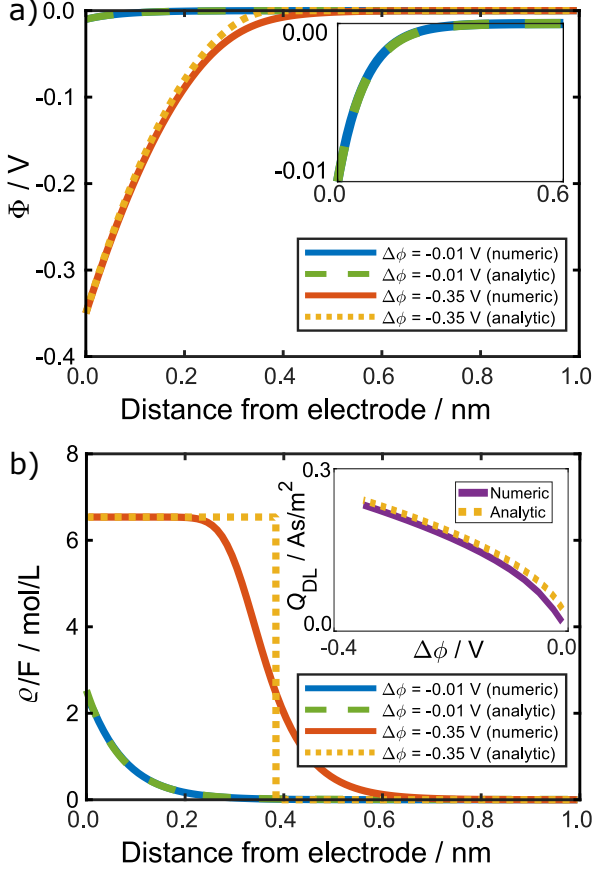
B. Asymptotic Analysis

FIG. 3. Comparison of the asymptotic analysis of the EDL structure with numeric results obtained from eqs. (43) and (46) ($T = 300$ K and $\varepsilon_R = 15$). We consider two different values of the interface potential, corresponding to the regimes of small and large potentials at $\Delta\phi = -0.01$ V ($\Delta\tilde{\phi} = -0.4$), and $\Delta\phi = -0.35$ V ($\Delta\tilde{\phi} = -13.5$). a) Profiles of the electric potentials as predicted by the analytic approximation (see eqs. (48) and (51)). The inset highlights the region close to the interface for the case $\Delta\phi = -0.01$ V. b) Profiles of the charge density as predicted by the asymptotic analysis in eqs. (49) and (53). The inset compares numeric and analytic values for the total charge comprised in the EDL (see section SI-3 C 2 in the SI).

The simulation results in section III A motivate our procedure for analysing the EDL structure. First, we study the EDL far away from the electrode close to the electroneutral bulk (large $\tilde{x}$). For this purpose, we expand the stationary equations around the electroneutral bulk for small charge densities, $\tilde{\varrho} \ll 1$. According to eq. (46), this regime corresponds to small dimensionless potentials $|\tilde{\Phi}| \ll 1$. Note that this coincides with the regime of high temperatures since $\tilde{\Phi} = \Phi \cdot Fz_+/RT$ (see section III B 1).

Second, we analyze the behavior close to the electrode (small $\tilde{x}$) at large electrode potentials $|\Delta\tilde{\phi}| \gg 1$, where the electrolyte potential satisfies $|\tilde{\Phi}| \gg 1$. This corresponds to small temperatures (see section III B 2).

1. Asymptotic Analysis: Small Potentials $|\tilde{\Phi}| \ll 1$

As outlined above, we begin our analytic examination of the EDL in the limit of small dimensionless potentials $|\tilde{\Phi}| \ll 1$. Our idea is to approach the EDL from the electroneutral bulk region along the direction of decreasing values $\tilde{x}$. Thus, we use the expansion of ionic concentrations around the bulk electrolyte in eq. (42), $\tilde{c}_\pm = \tilde{c}^b \pm \tilde{\varrho}\gamma_\mp \approx \tilde{c}^b$.

To this aim, we insert $\tilde{\varrho}$ from eq. (43) into eq. (44) for $\hat{\varepsilon}_R = 1$, yielding

$$\tilde{\nabla}^2 \tilde{\Phi} = \tilde{\Phi}. \tag{47}$$

With the boundary conditions discussed above, $\tilde{\Phi}(0) = \Delta\tilde{\phi} = Fz_+\Delta\phi/RT$ and $\tilde{\Phi}(\tilde{x} \to \infty) = 0$, we obtain the solution

$$\tilde{\Phi} = \Delta\tilde{\phi} \cdot \exp(-\tilde{x}), \tag{48}$$

$$\tilde{\varrho} = -\Delta\tilde{\phi} \cdot \exp(-\tilde{x}). \tag{49}$$

The corresponding dimensionalized electrolyte potential,

$$\Phi = \Delta\phi \cdot \exp(-x/L_D), \tag{50}$$

decays exponentially with damping parameter $1/L_D$. Thus, the decay length in the limit $|\tilde{\Phi}| \ll 1$ is the Debye length L_D (see eq. (29)).

In fig. 3, we compare the analytic predictions for this limit (dashed green lines) with the numeric results (blue lines) for different electrode potentials. Apparently, the analytic and numeric results for the electric potential and the charge density are in excellent agreement for small electrode potentials, $\Delta\tilde{\phi} \approx -0.4$, when the condition $|\tilde{\Phi}| \ll 1$ is fulfilled everywhere.

In the SI, we derive the expressions for the total EDL-surface-charge-density and the differential capacitance (see section SI-3 C 1).

2. Asymptotic Analysis: Large Potentials $|\tilde{\Phi}| \gg 1$

Next, we discuss the EDL in the limit of large potentials $|\tilde{\phi}| \gg 1$. This regime can be found for large electrode potentials $\Delta\tilde{\Phi} \gg 1$ close to the electrode/electrolyte interface. As $\tilde{\Phi} = Fz_+\Delta\phi/RT$, this analysis is exact in the limit of zero temperature, $T = 0$.

In this case, the logarithmic terms in eq. (46) must compensate the diverging potential term $\tilde{\Phi}$. Due to the mean volume constraint (see eq. (10)) one of the logarithmic terms is diverging if one species depletes and the other species saturates, $\varrho(x = 0) = Fz_{\alpha^*}/\nu_{\alpha^*}$. Here, we denote the saturating species by the index α^*. Since electric potentials are continuous across interfaces, the saturation species α^* is uniquely determined by the sign of the electrode potential, $\text{sign}(z_{\alpha^*}) = -\text{sign}(\Delta\tilde{\phi})$.

Therefore, $\tilde{\varrho}^{sat} = -\text{sign}(\Delta\tilde{\phi}) \cdot \tilde{c}^{sat}$ solves eq. (46), where $\tilde{c}^{sat} = \tilde{c}^b/\gamma_{\alpha^*}$. Upon integration of the Poisson eq. (43), we find

$$\tilde{\Phi}(\tilde{x}) = \Delta\tilde{\phi} \cdot \left(1 - \tilde{x}/\tilde{L}_{EDL}\right)^2, \tag{51}$$

where the width of the EDL depends on the electrode potential, $\tilde{L}_{\text{EDL}} = \sqrt{2\gamma_{\alpha^*}|\Delta\tilde{\phi}|/\tilde{c}^{\text{b}}}$. Thus, the dimensionalized EDL length is

$$L_{\text{EDL}} = L_{\text{D}} \cdot \tilde{L}_{\text{EDL}} = \sqrt{2a^3|\Delta\tilde{\phi}|\gamma_{\alpha^*}k_{\text{B}}T\varepsilon_0\varepsilon_{\text{R}}/(ez_+)^2} \quad (52)$$

Apparently, the decay length increases with ion size due to the mean-volume effect. Also, it scales with the asymmetry $\sqrt{\gamma_{\alpha^*}}$, *i.e.*, it is small for small screening species. Comparison with the Debye screening-length shows that $L_{\text{EDL}} > L_{\text{D}}$ in the limit of small temperatures T or large potentials $|\Delta\tilde{\phi}| \gg 1$.

In the limit of vanishing temperature, $T = 0$, the charge profile is box shaped and is determined by the screening-length L_{EDL},

$$\tilde{\varrho} = -\theta(\tilde{L}_{\text{EDL}} - \tilde{x}) \cdot \text{sign}(\Delta\tilde{\phi}) \cdot \tilde{c}^{\text{sat}}, \quad (53)$$

where θ is the Heaviside function. In the SI, we calculate the analytic expressions for the total charge in the EDL and for the differential capacitance in this limit (see section SI-3 C 2).

In fig. 3, we compare the analytic predictions for this limit (dashed yellow lines) with the numeric results (solid red lines) for $\Delta\tilde{\phi} = -13.5$. The box-shaped charge-profile is in good qualitative agreement with the numeric results, as it almost predicts the correct width of the EDL. However, the transition from saturation to the bulk-state is more diffuse in the numeric profile. This is due to the entropic, thermal influence, which "washes out" the box. Nevertheless, the inset shows that the charge comprised in the EDL, as predicted by the analytic approximation, is quantitatively in good agreement with the numeric results. We note that this profile and its temperature dependence is reminiscent of the Fermi distribution.

IV. NON-LOCAL INTERACTIONS: CHARGE OSCILLATIONS

In this section, we discuss the influence of non-local interactions ($\mathcal{V}^0 \neq 0$) on the structure of the EDL. As in section III, we discuss the two limiting cases of small and large potentials separately.

A. Static Asymptotic Analysis

1. Asymptotic Analysis: Large Potentials $|\tilde{\Phi}| \gg 1$

Let us first discuss the regime of diverging electrolyte potentials $|\tilde{\Phi}| \to \infty$. In this limit, the interaction contribution cannot compensate the diverging electrolyte potential in eq. (40). The logarithmic terms are diverging if one species depletes and we recover the same results as described in section III B 2 for the case of vanishing interaction contributions $\mathcal{V}^0 = 0$.

2. Asymptotic Analysis: Small Potentials $|\tilde{\Phi}| \ll 1$

In this section, we consider the full theory with molecular repulsion in the regime of small potentials $|\tilde{\Phi}| \ll 1$. As outlined above, we expand the interaction free energy in gradients of the charge density, and restrict our analysis to the first two perturbation modes $n = 0$ and $n = 1$. With the assumption of small charge densities $\tilde{\varrho} \ll 1$, we derived linear equations above (eqs. (43) and (44)), which we rephrase in matrix form,

$$\begin{pmatrix} \tilde{\nabla}^2\tilde{\varrho} \\ \tilde{\nabla}^2\tilde{\Phi} \end{pmatrix} = \tilde{\mathcal{A}} \cdot \begin{pmatrix} \tilde{\varrho} \\ \tilde{\Phi} \end{pmatrix}, \quad (54)$$

where

$$\tilde{\mathcal{A}} = \begin{pmatrix} \dfrac{\pi E_{\text{th}}^2}{2E_{\text{el}}\mathcal{V}^0}\left(1 - \dfrac{\mathcal{V}^0}{E_{\text{th}}}\right) & \dfrac{\pi E_{\text{th}}^2}{2E_{\text{el}}\mathcal{V}^0} \\ -1 & 0 \end{pmatrix}. \quad (55)$$

We solve eq. (54) via the eigenvalue decomposition with the eigenvalues $\tilde{\alpha}_{1,2}$ of the matrix eq. (55). These are determined by the relative magnitudes of the three competing energy scales, E_{th}, E_{el}, and $\mathcal{V}^0$,

$$\tilde{\alpha}_{1,2} = -\frac{\pi}{4} \cdot \frac{E_{\text{th}}}{E_{\text{el}}} \cdot \left[1 - \frac{E_{\text{th}}}{\mathcal{V}^0} \mp \sqrt{\left(1 - \frac{E_{\text{th}}}{\mathcal{V}^0}\right)^2 - \frac{8}{\pi} \cdot \frac{E_{\text{el}}}{\mathcal{V}^0}}\right]. \quad (56)$$

Each eigenvalue $\tilde{\alpha}_i$ gives rise to a dimensionless wave-vector,

$$\tilde{k}_{1,2} = \sqrt{\tilde{\alpha}_{1,2}}. \quad (57)$$

These determine the general solution of eq. (54) together with the eigenvectors $\tilde{\boldsymbol{a}}^{\tilde{\alpha}_i} = (\tilde{a}_1^{\tilde{\alpha}_i}, \tilde{a}_2^{\tilde{\alpha}_i})^T = (-\tilde{\alpha}_i, 1)^T$,

$$\begin{pmatrix} \tilde{\varrho} \\ \tilde{\Phi} \end{pmatrix} = \begin{pmatrix} \boldsymbol{a}^{\tilde{\alpha}_1} & \boldsymbol{a}^{\tilde{\alpha}_2} \end{pmatrix} \cdot \begin{pmatrix} A_1 e^{\tilde{k}_1\tilde{x}} + A_2 e^{-\tilde{k}_1\tilde{x}} \\ A_3 e^{\tilde{k}_2\tilde{x}} + A_4 e^{-\tilde{k}_2\tilde{x}} \end{pmatrix}. \quad (58)$$

The expansion coefficients A_i are determined by boundary conditions and physical arguments. Apparently, the corresponding wave-vectors are functions $\tilde{k}_{1,2}(T, z_\alpha, \varepsilon_{\text{R}}, \nu_\alpha, \mathcal{F}_{\alpha\beta})$, which determine the structure of the EDL,

$$\tilde{k}_{1,2} \in \begin{cases} \mathbb{R}, & \text{exponential damping,} \\ \mathbb{R} + \mathrm{i} \cdot \mathbb{R}, & \text{damped oscillations,} \\ \mathrm{i} \cdot \mathbb{R}, & \text{oscillations.} \end{cases}$$

Thus, the EDL structure depends upon the relative magnitudes of the energies E_{th}, E_{el}, and $\mathcal{V}^0$ via eq. (56). In particular, the classification of $\tilde{k}_\pm$ depends upon the sign of the root

$$\mathcal{W} = \left(1 - E_{\text{th}}/\mathcal{V}^0\right)^2 - 8E_{\text{el}}/\mathcal{V}^0\pi \quad (59)$$

appearing in eq. (56). Thus, the critical values $\mathcal{V}_\pm^0$, defined by the condition $\mathcal{W}(\mathcal{V}_\pm^0) = 0$, determine the thresholds for the transition between the phases of EDL structure,

$$\mathcal{V}_\pm^0 = E_{\text{th}} + 4E_{\text{el}}/\pi \pm 2\sqrt{2E_{\text{el}}(2E_{\text{el}}/\pi + E_{\text{th}})/\pi}. \quad (60)$$
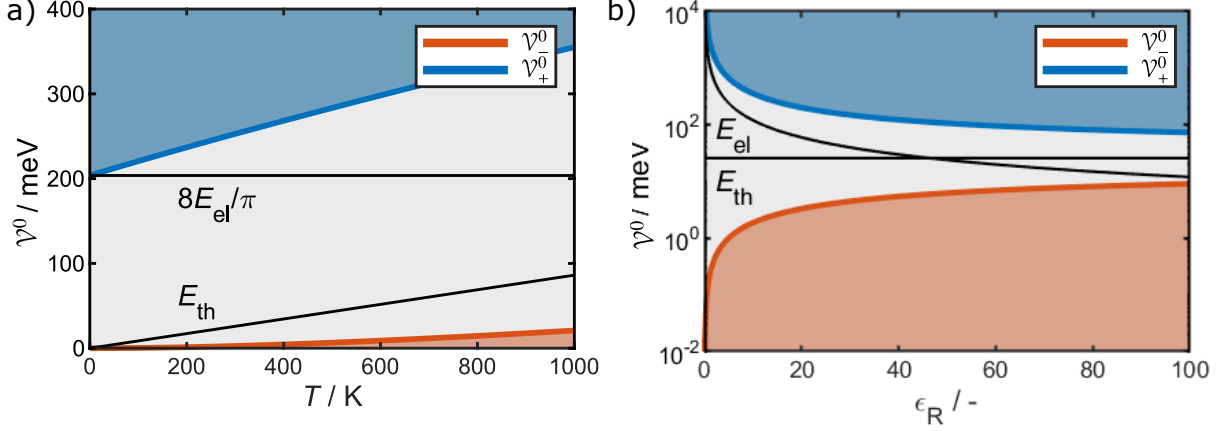
FIG. 4. Phase spaces for EDL structure as functions of T and ε_R for equally sized ions ($\gamma_\pm = 0.5$), see eq. (60). a) Critical interaction energies $\mathcal{V}_\pm^0$ as function of temperature (here, $\varepsilon_R = 15$, $a = 1.2\,\text{nm}$). b) Critical interaction energies $\mathcal{V}_\pm^0$ as function of dielectricity (here, $T = 300\,\text{K}$ and $a = 1.2\,\text{nm}$). Three phases are present: exponentially damped charge density (shaded red), decaying oscillatory charge density (shaded gray), quasi-crystalline (shaded blue).

Thus, with eq. (60) we can draw the phase diagram for the EDL structures. Since $0 < \mathcal{V}_-^0 < \mathcal{V}_+^0$, there are three phases. In the SI, we discuss each case in great detail (see section SI-3 D 2). Next, we give a short description of each phase.

Phase 1: $0 \leq \mathcal{V}^0 \leq \mathcal{V}_-^0$. In this regime, $\tilde{\alpha}_{1,2} \geq 0$, which implies a real-valued wave-vector. Thus, this phase corresponds to exponentially damped profiles, $\tilde{\varrho} \propto \exp(-\tilde{k}_R \tilde{x})$. A harmonic analysis of the root $\sqrt{\mathcal{W}}$ reveals that (see section SI-3 D 3)

$$\lim_{\mathcal{V}^0 \to 0} \tilde{k}_1 = \infty \quad \text{and} \quad \lim_{\mathcal{V}^0 \to 0} \tilde{k}_2 = 1. \tag{61}$$

Thus, solutions with the damping parameter $\tilde{k}_1$ vanish quickly and render unphysical, whereas the limit of vanishing interactions for $\tilde{k}_2$ reproduces the "bulk"-expansion for $\tilde{\Phi} \ll 1$ from section III B 1, see eq. (48).

Phase 2: $\mathcal{V}_-^0 < \mathcal{V}^0 < \mathcal{V}_+^0$. In this regime, $\mathcal{W} < 0$, and, thus, the root eq. (59) becomes complex. Therefore, the wave-vector has non-vanishing real and imaginary parts, $\tilde{k}_{1,2} \in \mathbb{R} \times i \cdot \mathbb{R}$. This corresponds to charge-profiles of exponentially damped oscillations,

$$\tilde{\varrho} \propto \exp(-\tilde{k}_R \tilde{x}) \cdot \cos(\tilde{k}_C \tilde{x}). \tag{62}$$

Phase 3: $\mathcal{V}_+^0 \leq \mathcal{V}^0$. In this regime, both eigenvalues are real but negative, $\tilde{\alpha}_{1,2} \leq 0$. Therefore, $k_\pm \in i \cdot \mathbb{R}$, which corresponds to undamped oscillatory profiles. The limiting case for indefinitely strong interactions yields

$$\lim_{\mathcal{V}^0 \to \infty} k_{1,2} = \lim_{\mathcal{V}^0 \to \infty} \tilde{k}_{1,2}/L_D = \begin{cases} 0, \\ \pm i \cdot 2\pi/a. \end{cases} \tag{63}$$

Thus, the result for $\lim_{\mathcal{V}^0 \to \infty} k_2$ reproduces the experimental findings obtained by AFM-measurements that the wavelengths $\lambda \approx a/2\pi$ of the observed oscillations scale with the size of molecules a.[52,64] Apparently, the incompressibility of
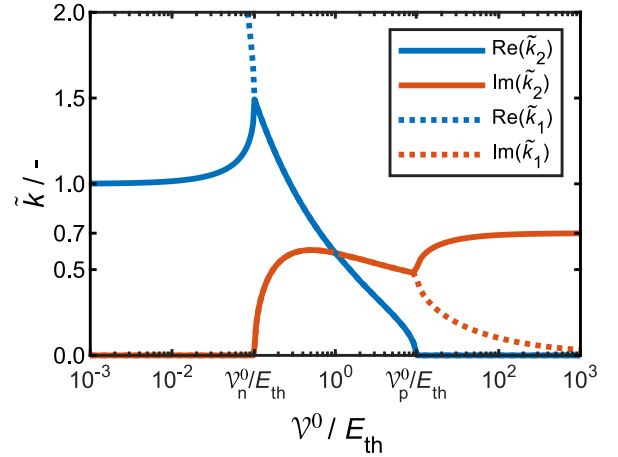

FIG. 5. Real and imaginary parts of the non-dimensionalized wave-vector $\tilde{k} = k \cdot L_D$ as function of the relative magnitude of the energy scales $\mathcal{V}^0$ and E_{th} (see eqs. (56) and (57)). Here, $T = 300\,\text{K}$, $\varepsilon_R = 15$, and $a = 1.2\,\text{nm}$.

ions in our model prevents a further decrease of the wavelength.

Thus, the critical values $\mathcal{V}_\pm^0$ constitute exactly the boundaries between the different EDL phases.

In fig. 4, we illustrate the phase space of EDL structures as functions of temperature and dielectricity (in section SI-6 A we also show the phase space as function of ion-size, ion-asymmetry and valency). Apparently, three distinct phases of EDL structures are present. Tthe exponentially damped EDL phase corresponds to the regions below $\mathcal{V}_-^0$ (red line), whereas the damped-oscillatory EDL phase corresponds to the regions between the blue and red lines. Finally, the undamped oscil-

latory EDL phase corresponds to the regions above $\mathcal{V}_+^0$ (blue line). Figure 4a illustrates that temperature T and hardcore-interactions $\mathcal{V}^0$ are in competition and the critical interaction strengths $\mathcal{V}_\pm^0$ increase with increasing temperature T, i.e., thermal energy E_{th}.

Figure 4b reveals the influence of dielectricity, i.e., electrostatic forces, on the EDL phases. Apparently, the damped oscillatory phase becomes narrower for ILs with larger dielectricity ε_R, i.e., smaller electric energy E_{el}.

We note that the exponentially damped regime for small interaction strengths (small compared to electrostatic and thermal energy) corresponds to the EDL structure found in section III B 1 in the absence of hardcore-interactions. However, as can be inferred from fig. 4a, this phase is hardly present for reasonable temperatures.

Figure 5 shows the non-dimensionalized wave-vector as function of the relative energy scale $\mathcal{V}^0/E_{th}$ (where T=300 K, ε_R=15, and a=1.2 nm). For small interaction energies $\mathcal{V}^0 < \mathcal{V}_-^0$ the wave-vector is real, $\tilde{k} = \tilde{k}_\mathbb{R}$, which corresponds to exponentially damped profiles. In particular, the static profile at $\mathcal{V}^0 \to 0$ reproduces the case described in section III B where the exponential profile is determined by the scales E_{th} and E_{el} alone, i.e. $\tilde{k} = 1$. Apparently, $\tilde{k}_\mathbb{R}$ increases with $\mathcal{V}^0$ up to the threshold $\mathcal{V}_-^0$, beyond which it starts to decrease. Thus, the EDL has minimal extension at $\mathcal{V}^0 = \mathcal{V}_-^0$. This suggests that the increasing strength of the repulsive ion-correlations compresses the screening-layer. Once the hardcore potential exceeds $\mathcal{V}_-^0$, the system overscreens, *i.e.*, the ion-layers begin to oscillate. The damping parameter $\mathrm{Re}(\tilde{k})$ vanishes exactly when $\mathcal{V}^0 = \mathcal{V}_+^0$, *i.e.*, when the system transitions into saturated nano-segregation of the ion species. Interestingly, the frequency of the oscillations $\mathrm{Im}(\tilde{k})$ exhibits a local maximum and minimum in the regime of damped oscillations. Furthermore, $\mathrm{Im}(\tilde{k})$ attains its maximal value in the limit of prevailing interaction strength $\mathcal{V}^0 \to \infty$.

In the SI (see sections SI-3 D 4 and SI-3 D 5) we investigate the influence of the individual perturbation modes Γ_{12}^0 and Γ_{12}^2 on the phase diagram. As it turns out, neglecting all but the zeroth-order correction Γ_{12}^0 results in a binary phase diagram comprising only exponentially damped profiles and undamped, oscillatory profiles. In contrast, neglecting the zeroth-order correction, and taking only the first non-trivial order Γ_{12}^2 into account, results in a binary phase-diagram comprising only exponentially damped profiles and damped oscillatory profiles. This is the case for MFTs based on the BSK-framework. Thus, for the "complete" set of the three different phases, both perturbation modes Γ_{12}^0 and Γ_{12}^2 are neccessary.

Interestingly, for the pathologic case of negative interaction-strengths $\mathcal{V}^0 < 0$, the phase space reduces to the two screening phases of exponentially damped profiles and undamped oscillatory profiles. This follows straightforwardly from eq. (56) (see also the discussions in sections SI-3 D 4 and SI-3 D 5).

B. Dynamic Asymptotic Analysis: Linear Stability Analysis

In this section, we complement the static analysis of section IV A by an analytic analysis of the dynamic transport equation in the gradient description (eq. (38)).

For this purpose, we perform a linear stability analysis and consider the limit of small potentials, $|\tilde{\Phi}| \ll 1$. Thus, the logarithmic terms can approximated as in eq. (42), and eq. (38) becomes

$$\partial_{\tilde{t}}\tilde{\varrho} = -\tilde{\nabla}^2\left(\tilde{\Phi} + \hat{\varepsilon}_R\tilde{\varrho}\right). \tag{64}$$

We expand the electric potential around an uniform bulk-state $\tilde{\Phi}^b$,

$$\tilde{\Phi} = \tilde{\Phi}^b + \sum_{i=1}^\infty \epsilon^i \cdot \tilde{\Phi}_i. \tag{65}$$

Here, the equilibrium state is determined by the electroneutral bulk-condition $\tilde{\Phi}^b = 0$ and $\tilde{\varrho}^b = 0$. Thus, the first order perturbation takes the form

$$\tilde{\Phi}_1 = \exp\left[\tilde{s}\tilde{t}\right] \cdot \cos\left[\tilde{k}\tilde{x}\right]. \tag{66}$$

Here, the wave-number $\tilde{k}$ determines the spatial distribution of the dimensionless perturbation $\tilde{\epsilon}^1 \ll 1$, and the parameter $\tilde{s}$ measures the temporal growth rate of this perturbation.

We restrict our analysis to probing the linear stability and substitute eq. (65) and the Poisson equation into eq. (64). Next, we collect terms up to the first order in the perturbation mode $\tilde{\epsilon}^1$, which yields a dispersion relation for the growth rate of the perturbation,

$$\tilde{s}(\tilde{k}) = -1 - \left(1 - \frac{\mathcal{V}^0}{E_{th}} + \frac{2}{\pi}\frac{\mathcal{V}^0}{E_{th}}\frac{E_{el}}{E_{th}}(\tilde{k})^2\right) \cdot (i\tilde{k})^2. \tag{67}$$

The uniform state is stable under perturbations if and only if $\tilde{s} < 0$. This defines an instability onset $\tilde{k}^c$ for the wave-numbers

$$\tilde{k}_{1,2}^c = \pm\frac{1}{2}\sqrt{\pi(\mathcal{V}^0 E_{th} - E_{th}^2)/E_{el}\mathcal{V}^0}. \tag{68}$$

The corresponding stability criterion $\tilde{s}(\tilde{k}_{1,2}^c)<0$ determines the phase boundary at which the bulk of the IL-electrolyte becomes unstable. This stability threshold equals exactly the phase boundary between the damped oscillatory phase and the nano-segregated phase (see eq. (60)),

$$\mathcal{V}_+^0 = E_{th} + 4E_{el}/\pi + 2\sqrt{2E_{el}(2E_{el}/\pi + E_{th})/\pi}. \tag{69}$$

Thus, for interaction energies $\mathcal{V}^0>\mathcal{V}_+^0$ the bulk state of the system becomes unstable and phase separation emerges. The initial cause for the structure-formation can be driven by external agents, or boundary conditions, e.g., by the application of an electric potential to an IL/electrode interface.

This stability analysis complements the static analysis, and rationalizes the emergence of phase separation into ionic layers occurring at interaction energies above $\mathcal{V}_+^0$.
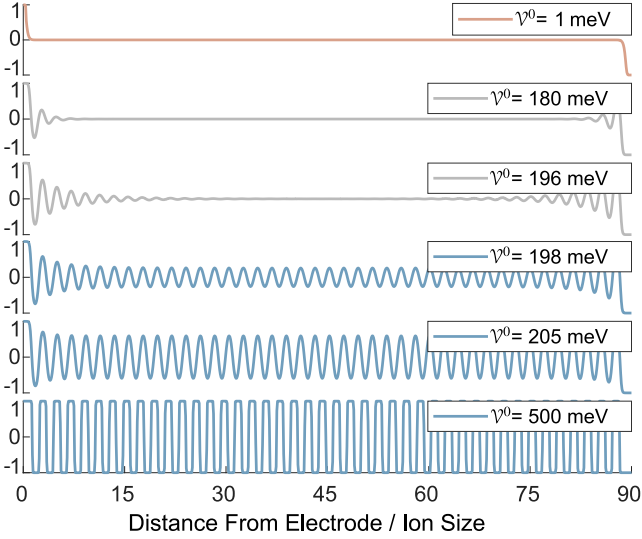
FIG. 6. Screening profiles of the charge density $\tilde{\varrho}$, as obtained from numerical simulations of the integral description (see eqs. (30) and (32)) for diferent values $\mathcal{V}^0$. The y-axis is scaled from -1 to 1, where $|\tilde{\varrho}| = 1$ corresponds to charge saturation.

C. Validation With Simulation

Our goal in this section is to compare the results of our asymptotic analysis (see eqs. (56) to (58) in section IV A 2), with numeric simulations of the completely-coupled system subject to the two theoretical descriptions (integral description eqs. (30) and (32), and gradient description eqs. (30) and (38)).

We start our numerical investigations with an overview of the screening profiles for the charge density at different values $\mathcal{V}^0$, as obtained from the integral description eqs. (30) and (32) (see fig. 6). Next, we compare our different EDL-descriptions in detail for two different energies $\mathcal{V}^0$, see figs. 7 and 8. Finally, we generalize these exemplary findings via a systematic study over the complete phase-space of interaction energies, see fig. 9. This provides a clear illustration of the complete set of phase-transitions which the system undergoes, and highlights the consistency between the three descriptions.

All simulations were performed for a symmetric cell setup, where the IL-electrolyte is located within two oppositely charged, blocking interfaces separated by a distance of $L_{\text{cell}} = 60$ nm. The electrode on the left side is negatively charged with $\Delta\phi = -100$ mV, whereas, on the right side, the electrode is positively charged with $\Delta\phi = 100$ mV. Since charge saturation begins roughly at $\Delta\phi = 70$ mV, see figs. 2 and 3, the charge distribution can safely be assumed saturated adjacent to the interfaces (i.e. $|\tilde{\varrho}| = 1$). The electrolyte is considered as consisting of symmetric ions ($\gamma_\pm = 0.5$) of size $a = 1.2$ nm. Hence, the cell-geometry allows a "maximal" number of roughly 100 ions. In addition, we assume room temperature, $T = 300$ K, and $\varepsilon_R = 15$. The phase boundaries corresponding to these parameters as predicted by our analytic description are $\mathcal{V}^0_- = 3$ meV and $\mathcal{V}^0_+ = 253$ meV (see eq. (60)).

Figure 6 shows numerical results of the charge density for the integral description (eqs. (30) and (32)), where $\mathcal{V}^0$ takes values across two orders of magnitude. First, at $\mathcal{V}^0 = 1$ meV the profile shows charge saturation near the two electrified electrodes, $\tilde{\varrho}(x{=}0) = 1$ and $\tilde{\varrho}(x{=}L_{\text{cell}}) = -1$. Near both electrodes, the profile decays exponentially towards the electroneutral bulk ($\tilde{\varrho} = 0$). This corresponds to the profiles which we discussed in great detail in section III A. Since $\mathcal{V}^0 < \mathcal{V}^0_-$, this is in accordance with the analytic prediction. The next two profiles show results for interaction energies within the intermediate phase, $\mathcal{V}^0_- < \mathcal{V}^0 < \mathcal{V}^0_+$. Both simulations show damped oscillatory profiles, where the long-ranged oscillatory profiles span across multiple nanometers. Apparently, the oscillations in the profile for $\mathcal{V}^0 = 196$ meV extend almost across the entire cell. A slight increase by 2 meV to $\mathcal{V}^0 = 198$ meV causes the profile to transition into a crystalline phase with undamped oscillatory shape. Note that the amplitudes between the electrodes are smaller than unity, i.e. the bulk region consists of mixed ion layers with one dominant ion species. An increase to $\mathcal{V}^0 = 204$ meV enhances the amplitudes of the oscillations further, i.e. enhances segregation of ion-species. The last plot shows the corresponding profile for a significantly enhanced interaction energy ($\mathcal{V}^0 = 500$ meV). Here, the amplitudes of the oscillations have reached saturation ($|\tilde{\varrho}| = 1$), and the electrolyte has transitioned into a crystalline phase consisting of alternating pure ion layers. In fig. SI-2 (see section SI-6 B), we highlight that the ionic layers coincide exactly with the ion size a. Thus, with increasing energies $\mathcal{V}^0$, the interfacial structure increases into the bulk electrolyte, until the bulk itself gets nanostrucured by layering of the ion species. This phase transition occurs rapidly within a few meV.

Apparently, the numeric results for the integral description confirm the existence of three different screening phases. However, quantitative deviation between our descriptions are present. As we show in the SI (see fig. SI-4) the phase transitions from exponential decay to damped oscillations occurs roughly at $\mathcal{V}^0 = 2$ meV. In addition, as can be inferred from fig. 6, the transition from damped oscillations to undamped oscillations appears at $\mathcal{V}^0 = 200$ meV. Hence, both phase boundaries are slightly shifted to smaller values, compared with the analytic prediction $\mathcal{V}^0_- = 3$ meV and $\mathcal{V}^0_+ = 253$ meV (see eq. (60)). Thus, the analytic prediction, which is based on the gradient description, slightly underestimates the influence of $\mathcal{V}^0$, when compared with E_{th} and E_{el}. This can be attributed to the fact that the gradient description is an approximation based on only the first two perturbation modes, whereas the integral description comprises all modes.

Next, we give a quantitative comparison between the numerical results of the two theoretical descriptions, and the analytic predictions. Here, we restrict our discussion to the interaction energy $\mathcal{V}^0 = 180$ meV, i.e. the intermediate phase of damped oscillations. Figure 7 shows the profiles for the charge density and electrolyte electric potential as obtained from the numeric simulations, and as predicted by the analytic description for the first few nanometers of the left half-cell. Figure 7a illustrates the charge distribution adjacent to the negatively charged electrode. The
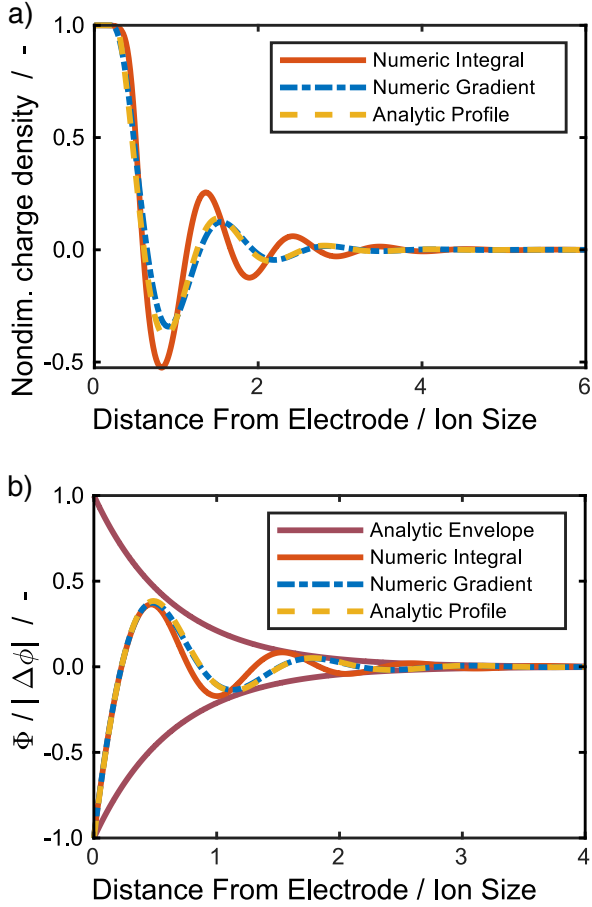
FIG. 7. Results for electric potential and charge density as obtained from numerical simulations of the integral description (eqs. (30) and (32)), and of the gradient description (eqs. (30) and (38)), and as predicted by the analytic predictions (see eqs. (56) to (58)) at $\mathcal{V}^0 = 180\,\text{meV}$.

dashed blue line shows the screening profile obtained from the gradient description, which exhibits a damped oscillatory shape. This confirms the analytic prediction for this interaction energy. The dashed yellow line shows the resulting analytic profile. Note that the analytic prediction in section IV does not capture charge-saturation, but only determines the damping-parameter and the oscillation-frequency of the screening-profile. However, in section III B 2, we derived an analytic prediction for the saturation-width L_{EDL}, valid close to the interface (see eq. (52)). Hence, in order to reconstruct the "complete" profile, we supplement the contribution emerging from the bulk eq. (58), valid far away from the interface, by constant charge-saturation $\tilde{\varrho} = 1$ spanning over the width L_{EDL}. Apparently, the analytic and numeric results of the gradient description are quantitatively in very good agreement. Finally, the solid red line in fig. 7a shows the numerical results for the integral description. In accordance with the results shown in fig. 6, these results reproduce the analytically predicted screening phase, but the oscillations are more pro-
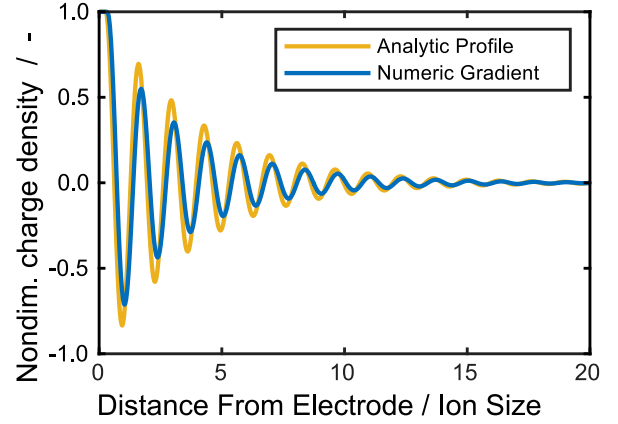

FIG. 8. Screening profile for the charge density $\tilde{\varrho}$ obtained from numerical simulations with respect to the gradient description (eqs. (30) and (38)), and according to the analytic description (see eqs. (56) to (58)), at $\mathcal{V}^0 = 250\,\text{meV}$.

nounced. Hence, the influence of the interaction energy $\mathcal{V}^0$ is more dominant in the integral description than in the gradient description. Next, in fig. 7b) we show the profiles for the normalized electrolyte electric potential. The dashed blue line shows the profile due to the gradient description. It is in accordance with the charge-profile shown in fig. 7a, see also eqs. (42) and (43). Again, we reconstruct the analytic profile by supplementing the profile eq. (51), valid close to the interface, by the profile eq. (58), valid towards the electroneutral bulk. Apparently, the analytic results are quantitatively in very good agreement with the results stemming from the gradient description. The red line shows the profile as obtained from the integral description. Like in fig. 7a for the charge density, the oscillations are slightly enhanced when compared with the gradient description. In addition, the brown solid lines show the analytic envelopes for the screening. Apparently, it captures both numerical results qualitatively very well. Interestingly, the differences in electrolyte potential between the three descriptions depend on electrode potential near the electrode as shown in fig. SI-3 (see section SI-6 C). However, the qualitative agreement is independent from the boundary conditions.

In fig. 8, we show results for the charge distribution at enhanced interaction energy $\mathcal{V}^0 = 250\,\text{meV}$, i.e., close to the phase boundary $\mathcal{V}_+^0 = 253\,\text{meV}$. As can be inferred from fig. 6, the integral description has already transitioned to the phase of undamped oscillations for this interaction energy. Hence, we only show the screening profile as obtained from numerical simulation of the gradient description (solid blue line), and compare it with the analytic prediction (yellow line). Apparently, in accordance with the analytic prediction, the numerical profile has a damped oscillatory shape, where the oscillations extend over roughly 20 ion sizes. This highlights the influence of the enhanced interaction energy, see also fig. 7. Overall, the analytic profile shown here is in nice agreement with the numeric results.

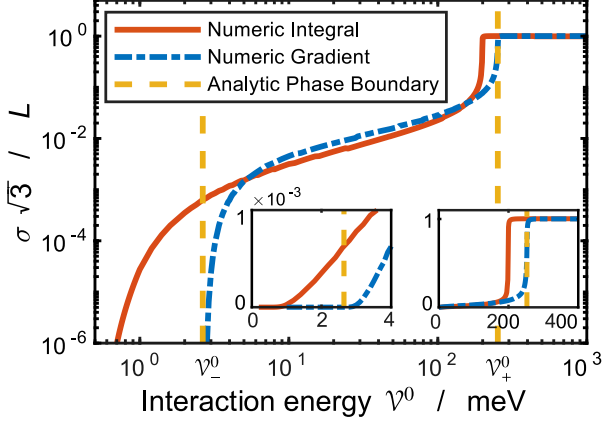Finally, we conduct a quantitative comparison between the

FIG. 9. Meta analysis of the interfacial profiles for some thousand simulations. The dashed vertical yellow lines show the phase boundaries $\mathcal{V}_{\pm}^0$ (see eq. (60)). The dashed and solid red / blue lines show the peak-variance of the complete set of simulations as defined by eq. (70), with respect to the integral description (see eqs. (30) and (32)), and with respect to the gradient-description (see eqs. (30) and (38)). The left inset shows the onset of the oscillations at small interaction energies. The right inset shows the variance in a non-logarithmic setting, which highlights the occurrence of phase-transitions.

two EDL-discriptions and the analytic description across multiple orders of magnitude of $\mathcal{V}^0$. To address this goal, we examine simulation results of roughly 4000 EDL-simulations across the parameter range from $0.1\,\mathrm{meV}$ up to $500\,\mathrm{meV}$. As above, we apply $\Delta\phi = \pm 100\,\mathrm{meV}$ at the electrodes such that we can safely assume charge saturation near the interfaces.

We evaluate the simulation results by extracting two characteristic properties. First, we count the number of peaks $N_{\mathrm{peaks}}(\mathcal{V}^0)$ appearing in each screening profile. Due to charge saturation, a minimal number of two peaks always occurs. At most, roughly 90 ion-layers fit into the cell geometry of length $L_{\mathrm{cell}} = 60\,\mathrm{nm}$. We present the number of peaks occurring in the full cell as function of the interaction strengths in the SI (see fig. SI-4 in section SI-6).

However, beyond the number of peaks, we want to evaluate the peak amplitudes, too. For this purpose, we investigate the peak variance $\sigma(\mathcal{V}^0)$ of the left half-cell, defined by

$$\sigma^2 = \frac{\sum_{i=1}^{N_{\mathrm{peaks}}} \tilde{\varrho}_i \cdot (\tilde{x}_i)^2}{\sum_j^{N_{\mathrm{peaks}}} \tilde{\varrho}_j}. \qquad (70)$$

Here, $\tilde{x}_i$ is the discrete location of the i-th peak $\tilde{\varrho}_i = |\tilde{\varrho}(\tilde{x}_i)|$ (such that $0 \leq \tilde{\varrho}_i \leq 1$, where $\tilde{\varrho}_i = 1$ corresponds to a saturated peak, i.e. a pure ion-layer) appearing in the profile of the charge density. In the SI (see section SI-6 D), we show analytically that σ converges to $L_{\mathrm{cell}}/\sqrt{3}$ if the set of simulation-energies comprises energies $\mathcal{V}^0 \gg \mathcal{V}_+^0$. For such interaction energies, the bulk electrolyte has transitioned into a crystalline phase composed of nano-segregated ion-layers (see fig. 6).

Figure 9 shows the results for variance σ^2 normalized to its maximum $L_{\mathrm{cell}}/\sqrt{3}$ in logarithmic scale. In this figure, the vertical dashed yellow lines indicate the phase-boundaries $\mathcal{V}_{\pm}^0$, as predicted by the analytic description (see eq. (60)). The left inset shows the simulation-results for small values $\mathcal{V}^0$, and the right inset comprises the overall results in a non-logarithmic representation highlighting the transition. The blue dashed line shows the results for σ according to the gradient description (see eqs. (30) and (38)). At small interaction energies $\mathcal{V}^0 < \mathcal{V}_-^0$, the variance is zero. This corresponds to an exponentially damped, non-oscillatory screening profiles (note that the only peak, due to charge saturation, is located at $\tilde{x}_i = 0$). The variance starts increasing exactly at $\mathcal{V}_-^0$ (see also the left inset). This corresponds to an increasing number of damped oscillations, where the amplitudes of the peaks also increase with $\mathcal{V}^0$. Finally, at $\mathcal{V}_+^0$, the variance converges to it's constant limiting value $L_{\mathrm{cell}}/3$ (see also the right inset). In this energy-regime, the bulk electrolyte consists completely of pure ion-layers. Altogether, these results reproduce exactly the phases as predicted by the analytic description.

The red curve shows the results for σ according to the integral description (see eqs. (30) and (32)). In contrast to the gradient description, the variance starts increasing from zero at roughly $\mathcal{V}^0 = 1\,\mathrm{meV}$, i.e. before the analytically predicted phase boundary $\mathcal{V}_-^0$ (see also the left inset). Hence, the phase transition from exponentially damped screening-profiles to damped oscillatory screening-profiles is slightly shifted to smaller energies. Next, the variance increases exponentially up to roughly $\mathcal{V}^0 = 200\,\mathrm{meV}$, above which it transitions into the constant limiting value $L_{\mathrm{cell}}/3$. Altogether, the phase boundaries of the integral description still exhibit a qualitatively good agreement with the analytic predictions, although being slightly shifted to smaller values. Apparently, this behaviour is due to the cumulative effect of the integral-term in eq. (32), which comprises all interaction modes. In contrast, we consider only the first two modes (n=0 and n=1) of the gradient expansion in eq. (38).

V. MULTI-SCALE METHODOLOGY

In this section, we highlight the relation of our model to theories on smaller and larger length scales. We discuss in section V A, based on basic concepts from liquid state theory, how atomistic simulations can directly parametrize our theory. Next, in section V B we sketch the phenomenologic BSK continuum approach for the description of ILs near electrified interfaces and illustrate its relation to our work. In addition, we state the relation of our framework to AFM-experiments in the section SI-5 (see also Ref. 52).

A. From Molecular Dynamics to Non-Equilibrium Thermodynamics

Here, we explain how the parameters of our continuum theory can be rigorously calculated with quantum chemistry, i.e., DFT and MD.

Ab-initio DFT calculations predict the forces between ions and molecules by calculating their electronic structure. The DFT-generated force-fields are the focal quantity for MD simulations,[65] which calculate the classical trajectories of ions and molecules. Results from MD simulations are often interpreted via profiles of the radial distribution function $g(r)$.

Liquid state theory,[50] connects this atomistic description to thermodynamic concepts and scattering experiments.[66] On the one hand, the radial distribution function allow a straightforward comparison with the structure factor S from scattering experiments.[67,68] On the other hand, the density distribution function $g(r)$ can be used to calculate different correlation functions. By subtracting its asymptotic value follows the so-called total correlation function used in integral equation theories (IETs), $h(r) = g(r) - 1$.[3] In IETs, the pairwise total correlation function h relates to the the direct correlation function $c^{(2)}$, used in classical density functional theory (cDFT), via the Ornstein-Zernike relation,[69]

$$h(r) = c^{(2)} + \rho_{\text{b}} \int \mathrm{d}r' c^{(2)}(|r - r'|) \cdot h(r'). \qquad (71)$$

In cDFT, the direct pair correlation functions $c^{(2)}_{\alpha\beta}$ account for pairwise interactions between two ions of species α and β, *i.e.*, the excess free energy due to pairwise ion-interactions.[70] Thus, they can be obtained via the twofold functional derivative of F^{int},[66] *i.e.*, via our interaction potential $\mathcal{F}$ (see eq. (15)),

$$c^{(2)}_{\alpha\beta}(|r - r'|) = -\frac{1}{k_{\text{B}}T(N_{\text{A}})^2} \cdot \mathcal{F}_{\alpha\beta}(|r - r'|). \qquad (72)$$

To summarize, DFT determines force fields for MD, MD determines $g(r)$ for liquid state theory, $g(r)$ determines $c^{(2)}$ via the Ornstein-Zernike relation, $c^{(2)}$ determines F^{int} and generates our non-equilibrium thermodynamic theory.

The dynamic properties of our theory can be determined from atomistic simulations, too. These dynamic properties are encoded in the Onsager coefficients,[45] which can be measured experimentally.[71] The Onsager coefficients can be determined by MD simulations ("Green Kubo relations").[72–74]

B. From Non-Equilibrium Thermodynamics to Phenomenologic BSK Theory

Now, we compare our thermodynamically consistent continuum approach with the phenomenologic theory proposed by Bazant, Storey, and Kornyshev (BSK), a seminal MFT-approach for ILs near electrified interfaces.[35] In their continuum model of the EDL, BSK incorporate ion-correlations using a modified linear dielectric relation $\bar{\boldsymbol{D}} = \hat{\bar{\varepsilon}}\boldsymbol{E}$ between the electrostatic fields $\bar{\boldsymbol{D}}$ and $\boldsymbol{E}$, where $\hat{\bar{\varepsilon}} = \varepsilon_{\text{R}}\varepsilon_0(1 - \ell_{\text{c}}\nabla^2)$ is their dielectric operator. The second order gradient term in $\bar{\varrho}$ accounts for non-local ion-interactions, being effectively short-ranged with correlation length ℓ_{c}. This Ansatz yields a modified Poisson equation, $\hat{\bar{\varepsilon}}\nabla^2\Phi = -\bar{\varrho}$. The chemical potential connects electric potential and charge density. Finally,

$$\hat{\bar{\varepsilon}}\nabla^2\Phi = \Phi. \qquad (73)$$

holds in the limit of small potentials $\tilde{\Phi}$.

Our model conceptually differs from BSK theory. Since we incorporate electrostatic correlations in the free energy, non-local ion-interactions enter the set of equations via the chemical potentials. This implies that the MFT-quantities appearing in the BSK description, $\bar{\boldsymbol{D}}$ and $\bar{\varrho} = \nabla\bar{\boldsymbol{D}}$, differ from the corresponding quantities ϱ and $\boldsymbol{D}$ appearing in our formalism. In contrast to the "mean field charge density" $\bar{\varrho}$, the charge density ϱ relates to the "bulk"-quantity $\boldsymbol{D}$, which does not incorporate ion correlations.

Despite these differences, the resulting model equations are very similar. This can be seen as follows. The complete set of equations eqs. (43) and (44) for the limit of small potentials can be cast into one equation for the electric potential alone,

$$\hat{\varepsilon}_{\text{R}}\tilde{\nabla}^2\tilde{\Phi} = \tilde{\Phi}, \qquad (74)$$

where the dielectric operator $\hat{\varepsilon}_{\text{R}}$ is defined in eq. (45). Noting the conceptual similarity between the dielectric operators $\hat{\varepsilon}_{\text{R}}$ and $\hat{\bar{\varepsilon}}$, the similarity between our model and BSK theory becomes apparent. In this way, we give physical meaning to the correlation length ℓ_{c} in BSK theory and outline its calculation.

Finally, we emphasize that the higher-order gradient-terms, which are phenomenologically incorporated in the BSK approach, emerge naturally within our rigorous continuum model. In particular, they merely constitutes the limiting case for small potentials of the more fundamental integral formulation eq. (41). Furthermore, in contrast to the phenomenological BSK model, our order-expansion comprises also a zero-order correction in the dielectric operator, see eq. (45). This mode is mandatory to realize the "complete" phase-space of interfacial profiles (see sections SI-3 D 4 and SI-3 D 5 in the SI).

VI. CONCLUSION

In this work, we complement our thermodynamically consistent continuum framework for IL electrolytes by non-local molecular repulsion. Our integral formulation can be determined by ab-initio MD simulations. Assuming short-ranged interactions, we expand the interaction free energy in gradients of the concentrations and adjust the dynamic equations for transport. The resulting equations connect to the phenomenologic approach of BSK theory. We validate our approach by simulations and find a remarkable agreement between the different variants of our theory.

In this way, we develop a predictive multi-scale approach to the theory of ILs at electrified interfaces. Atomistic density functional theory calculations parameterize MD simulations, MD simulations yield an integral formulation for molecular repulsion in our thermodynamic consistent transport theory, our theory can be expanded to give the phenomenological BSK theory.

The expanded continuum approach allows to perform analytic asymptotic analysis which creates deeper insights into parameter dependence of EDL structure as we demonstrate for the example of binary ILs. First, we have neglected molecular repulsion. We can analytically describe both limits, the dilute Debye limit, where charge density is exponentially decaying,

and the concentrated crowding limit, where charge is saturated due to steric effects. Second, we have taken into account molecular repulsion. We discuss the structure of the EDL dependent on energy scales for thermal motion, molecular repulsion, and electric Coulomb forces and find three different phases. For small interactions, we recover the dilute Debye limit. For intermediate interactions, a multi-layer structure of ions emerges which is washed out over several atom layers. For very large interactions, the analysis predicts a long-ranged, non-decaying crystalline order of the EDL. In simulations of our full theory, we eventually observe charge ordering of quasi-crystalline multi-layers in this case.

In summary, we have proposed a thermodynamic consistent description of ILs at electrified interfaces that closes a gap in their multi-scale understanding. This makes possible a predictive theoretical approach for tailoring ILs. We proof that the inter-molecular forces determine the EDL structure of binary ILs. Future works should extend the work to ternary mixtures of ILs and incorporate the shape of molecules into the theory.

[1] B. Eisenberg, Biophysical journal **104**, 1849 (2013).
[2] A. Y. Grosberg, T. Nguyen, and B. Shklovskii, Reviews of modern physics **74**, 329 (2002).
[3] D. Henderson, Interdisciplinary sciences: computational life sciences **1**, 1 (2009).
[4] Y.-G. Chen and J. D. Weeks, Proceedings of the National Academy of Sciences **103**, 7560 (2006).
[5] V. A. Bloomfield, Biopolymers: Original Research on Biomolecules **31**, 1471 (1991).
[6] G. C. Wong and L. Pollack, Annual review of physical chemistry **61**, 171 (2010).
[7] B. Eisenberg, Y. Hyon, and C. Liu, The Journal of Chemical Physics **133**, 104104 (2010).
[8] M. E. Fisher and Y. Levin, Physical review letters **71**, 3826 (1993).
[9] Y. Levin and M. E. Fisher, Physica A: Statistical Mechanics and its Applications **225**, 164 (1996).
[10] R. van Roij and J.-P. Hansen, Physical review letters **79**, 3082 (1997).
[11] J.-P. Hansen and H. Löwen, Annual Review of Physical Chemistry **51**, 209 (2000).
[12] Y. Levin, Reports on progress in physics **65**, 1577 (2002).
[13] E. Hückel, in Ergebnisse der exakten naturwissenschaften (Springer, 1924) pp. 199–276.
[14] M. S. Kilic, M. Z. Bazant, and A. Ajdari, Phys. Rev. E **75**, 021502 (2007).
[15] R. Hayes, G. G. Warr, and R. Atkin, Chemical Reviews **115**, 6357 (2015).
[16] D. W. Bruce, C. P. Cabry, J. N. Canongia Lopes, M. L. Costen, L. D'Andrea, I. Grillo, B. C. Marshall, K. G. McKendrick, T. K. Minton, S. M. Purcell, S. Rogers, J. M. Slattery, K. Shimizu, E. Smoll, and M. A. Tesa-Serrate, The Journal of Physical Chemistry B **121**, 6002 (2017).
[17] M. V. Fedorov and A. A. Kornyshev, Chemical reviews **114**, 2978 (2014).
[18] N. V. Plechkova and K. R. Seddon, Chemical Society Reviews **37**, 123 (2008).
[19] J. F. Wishart, Energy Environ. Sci. **2**, 956 (2009).
[20] T. Torimoto, T. Tsuda, K.-i. Okazaki, and S. Kuwabata, Advanced Materials **22**, 1196 (2010).
[21] S. Werner, M. Haumann, and P. Wasserscheid, Annual review of chemical and biomolecular engineering **1**, 203 (2010).
[22] T. Welton, Chemical reviews **99**, 2071 (1999).
[23] F. Endres, Zeitschrift für Physikalische Chemie **218**, 255 (2004).
[24] M. Armand, F. Endres, D. R. MacFarlane, H. Ohno, and B. Scrosati, in Materials For Sustainable Energy (World Scientific, 2011) pp. 129–137.
[25] F. Endres, O. Höfft, N. Borisenko, L. H. Gasparotto, A. Prowald, R. Al-Salman, T. Carstens, R. Atkin, A. Bund, and S. Z. El Abedin, Physical Chemistry Chemical Physics **12**, 1724 (2010).
[26] D. R. MacFarlane, J. M. Pringle, P. C. Howlett, and M. Forsyth, Physical Chemistry Chemical Physics **12**, 1659 (2010).
[27] J. Wu, T. Jiang, D.-e. Jiang, Z. Jin, and D. Henderson, Soft Matter **7**, 11222 (2011).
[28] D. Henderson and J. Wu, The journal of physical chemistry B **116**, 2520 (2012).
[29] J. Jiang, D. Cao, D.-e. Jiang, and J. Wu, Journal of Physics: Condensed Matter **26**, 284102 (2014).
[30] S. Sharma, A. Gupta, and H. K. Kashyap, The Journal of Physical Chemistry B **120**, 3206 (2016).
[31] S. Sharma and H. K. Kashyap, The Journal of Physical Chemistry C **119**, 23955 (2015).
[32] Z. Hu, J. Vatamanu, O. Borodin, and D. Bedrov, Physical Chemistry Chemical Physics **15**, 14234 (2013).
[33] J. Bikerman, The London, Edinburgh, and Dublin Philosophical Magazine and Journal of Science **33**, 384 (1942).
[34] C. D. Santangelo, Physical Review E **73**, 041512 (2006).
[35] M. Z. Bazant, B. D. Storey, and A. A. Kornyshev, Phys. Rev. Lett. **106**, 046102 (2011).
[36] A. Yochelis, Physical Chemistry Chemical Physics **16**, 2836 (2014).
[37] A. Yochelis, The Journal of Physical Chemistry C **118**, 5716 (2014).
[38] A. Yochelis, M. B. Singh, and I. Visoly-Fisher, Chemistry of Materials **27**, 4169 (2015).
[39] N. Gavish and A. Yochelis, The Journal of Physical Chemistry Letters **7**, 1121 (2016).
[40] S. Bier, N. Gavish, H. Uecker, and A. Yochelis, Phys. Rev. E **95**, 060201 (2017).
[41] A. A. Lee, S. Kondrat, D. Vella, and A. Goriely, Phys. Rev. Lett. **115**, 106101 (2015).
[42] N. Gavish, D. Elad, and A. Yochelis, The Journal of Physical

[43] Chemistry Letters **9**, 36 (2018).
[43] D. Bothe and W. Dreyer, Acta Mechanica **226**, 1757 (2015).
[44] A. Kovetz, Electromagnetic theory, Vol. 975 (Oxford University Press Oxford, 2000).
[45] M. Schammer, B. Horstmann, and A. Latz, Journal of the Electrochemical Society **168**, 026511 (2021).
[46] A. Latz and J. Zausch, Beilstein journal of nanotechnology **6**, 987 (2015).
[47] T. Schmitt, T. Arlt, I. Manke, A. Latz, and B. Horstmann, Journal of Power Sources **432**, 119 (2019).
[48] K. Becker-Steinberger, S. Schardt, B. Horstmann, and A. Latz, arXiv , 2101.10294 (2020), arXiv:2101.10294.
[49] F. Single, B. Horstmann, and A. Latz, The Journal of Physical Chemistry C **123**, 27327 (2019).
[50] J. Hansen and I. McDonald, Theory of Simple Liquids (Elsevier Science, 2006).
[51] M. Landstorfer, C. Guhlke, and W. Dreyer, Electrochimica Acta **201**, 187 (2016).
[52] V. Hoffmann, G. Pulletikurthi, T. Carstens, A. Lahiri, A. Borodin, M. Schammer, B. Horstmann, A. Latz, and F. Endres, Phys. Chem. Chem. Phys. **20**, 4760 (2018).
[53] M. Van Dijk and A. Wakker, Concepts in polymer thermodynamics, Vol. 2 (CRC Press, 1998).
[54] D. Bothe, W. Dreyer, and P.-E. Druet, Multicomponent incompressible fluids – an asymptotic study (2021), arXiv:2104.08628.
[55] D. Bedrov, J.-P. Piquemal, O. Borodin, A. D. MacKerell, B. Roux, and C. Schröder, Chemical Reviews **119**, 7940 (2019).
[56] H. Heinz, T.-J. Lin, R. Kishore Mishra, and F. S. Emami, Langmuir **29**, 1754 (2013).
[57] B. Eisenberg, Y. Hyon, and C. Liu, Communications in Mathematical Sciences **9**, 459 (2011).
[58] T.-C. Lin and B. Eisenberg, Communications in Mathematical Sciences **12**, 149 (2014).
[59] T.-C. Lin and B. Eisenberg, Nonlinearity **28**, 2053 (2015).
[60] A. A. Lee, C. Perez-Martinez, A. M. Smith, and S. Perkin, Faraday Discussions **199**, 239 (2017), 1701.08151.
[61] B. Rotenberg, O. Bernard, and J.-P. Hansen, Journal of Physics: Condensed Matter **30**, 054005 (2018).
[62] K. Karuppasamy, J. Theerthagiri, D. Vikraman, C.-J. Yim, S. Hussain, R. Sharma, T. Maiyalagan, J. Qin, and H.-S. Kim, Polymers **12**, 918 (2020).
[63] W. Schmickler and E. Santos, Interfacial electrochemistry (Springer Science & Business Media, 2010).
[64] H. Li, F. Endres, and R. Atkin, Physical Chemistry Chemical Physics **15**, 14624 (2013).
[65] González, M.A., JDN **12**, 169 (2011).
[66] H. V. Beijeren and B. Felderhof, Molecular Physics **38**, 1179 (1979).
[67] S. J. L. Billinge, Philosophical Transactions of the Royal Society A: Mathematical, Physical and Engineering Sciences **377**, 20180413 (2019).
[68] E. I. Kats and A. R. Muratov, Phys. Rev. E **97**, 012610 (2018).
[69] A. J. Archer, B. Chacko, and R. Evans, The Journal of Chemical Physics **147**, 034501 (2017).
[70] S. Cao, K. A. Konovalov, I. C. Unarta, and X. Huang, Advanced Theory and Simulations **2**, 1900049 (2019).
[71] K. D. Fong, J. Self, B. D. McCloskey, and K. A. Persson, Macromolecules **54**, 2575 (2021).
[72] K. D. Fong, H. K. Bergstrom, B. D. McCloskey, and K. K. Mandadapu, AIChE Journal **66**, e17091 (2020).
[73] W. Gotze and A. Latz, Journal of Physics: Condensed Matter **1**, 4169 (1989).
[74] A. Latz, Verallgemeinerte konstituierende gleichungen und formfaktoren für einfache glasbildner (1991), dissertation TU München.